Founded 1905

SYNTHESIS AND CHARACTERIZATION OF CaF$_2$:Yb,Er (CORE) /CaF$_2$ (SHELL) UP-CONVERSION NANOPARTICLES

LIU ZHENGYI

(B.Eng)

A THESIS SUBMITTED

FOR THE DEGREE OF MASTER OF ENGINEERING

DEPARTMENT OF MATERIALS SCIENCE AND ENGINEERING

NATIONAL UNIVERSITY OF SINGAPORE

2010

Acknowledgements

First of all, I want to express my sincere thanks to my supervisor Prof. Chow Gan Moog for his guidance and inspiration all along the way. Apart from the knowledge I have gained from him, he has always been training me to think critically, work systematically and independently. I believe I will benefit from those habits not only in my study but also in my future life.

I also want to thank Dr. Yi Guangshun for sharing his own research experiences and tips without reservation. I am truly grateful to Mr. Yuan Du, Mr. Qian Lipeng, Mr. Karvianto and Dr. Liu Min for their valuable help and fruitful discussions.

Thanks for the technical supports from Dr. Zhang Jixuan, Mrs. Yang Fengzhen, Ms. LIM, Mui Keow Agnes, Mr. Chen Qun and Mr. Henche Kuan. The financial support provided by the National University of Singapore is also acknowledged.

Last but not least, I want to thanks the mental support of my parents and friends like: Wang Hongyu, Luo Wei, Liu Huajun, Yuan Jiaquan, Xu Fan and Yun Jia who always cheer me up to overcome the difficulties in this journey.

Contents

Summary

The synthesis of monodispersed CaF_2:Yb,Er up-conversion nanoparticles (particle size ~ 5.4 nm ± 0.9 nm) using thermolysis of precursors in oleylamine at 340 ^{o}C was studied. These nanoparticles were characterized using TEM, XRD, FTIR, Zeta potential, DTA/TGA and XPS.

An undoped CaF_2 shell was subsequently deposited on the doped core nanoparticles to form the CaF_2:Yb,Er(core)/CaF_2(shell) structure in order to improve the emission intensity. The critical shell thickness was determined to be ~ 2.5 nm which improved the emission intensity by more than 20 times. Both core and core/shell nanoparticles were stable in solvents such as chloroform and hexane.

By conducting a series of comparative experiments, the improvement of the emission intensity was mainly attributed to the decrease of surface-to-volume ratio of the RE doped nanoparticles. Amorphous silica coating on CaF_2:Yb,Er(core)/CaF_2(shell) UCNPs was also achieved to demonstrate the potential for bio-application.

CaF_2:Yb,Er(core)/CaF_2(shell) up-conversion nanoparticles showing strong red emission, with its longer wavelength and penetration distance compared with that of shorter wavelengths of green and blue lights, may find promising potential applications.

Keywords: CaF_2, rare-earth doping, up-conversion, core-shell structure, near infrared, thermal decomposition, silica coating

List of Tables

List of Figures

Chapter 1

1 Introduction

1.1 Up-conversion luminescence

1.1.1   Different up-conversion processes

The idea of up-conversion (UC) process can be traced back to 1959 in the proposal of infrared quantum counter (IRQC) by Bloembergen [1]. It was until 1966, that the general concept and the role of energy transfers in UC processes was formulated by Auzel [2]. It is a nonlinear optical process of emitting a high energy photon by the absorption of two or more low energy photons. The UC process can be divided mainly into three classes: energy transfer up-conversion (ETU), photon avalanche (PA), and excited state absorption (ESA) [3].

ESA is the simplest UC process as illustrated by a three-level system in **Figure 1.1** A. It is a sequential absorption of two or more excited photons at a single rare earth (RE) ion. The ground state absorption (GSA) occurs when the energy of excitation photon resonates with the transition from the ground state (G) to first excited state (E_1). By absorbing the other pumping photon, the electrons of the RE ions is further excited to second excited state (E_2). Then,

they give out UC emission.

The difference between ETU and ESA is that the excitation process involves at least two RE ions in ETU (**Figure 1.1** B). The distance between the neighbour ions should be close enough to enable the energy transfer process (~ 1 nm) [4]. Both RE ions can absorb the pumping photons to populate the state of E_1. After undergoing a non-radiative energy transfer, one of the ions reaches the E_2 state while the other ion relaxes to the ground state. This energy transfer process enables the ETU to be more efficient than ESA process.

The unique feature of PA process is that it requires the pump intensity to be above a certain level to yield UC luminescence (**Figure 1.2**). Unlike the ESA which starts with energy-resonant GSA, the PA starts with very weak GSA, the excited electrons are then pumped to the E_2 state. Without emitting photon immediately, it undergoes a cross-relaxation process to transfer part of its energy to the neighbouring ions resulting in both the ions staying in the E_1 energy level. After that, both of them will be pumped to E_2 state. This process will be repeated several times until the E_2 population becomes high enough to produce UC emission (**Figure 1.1** C).
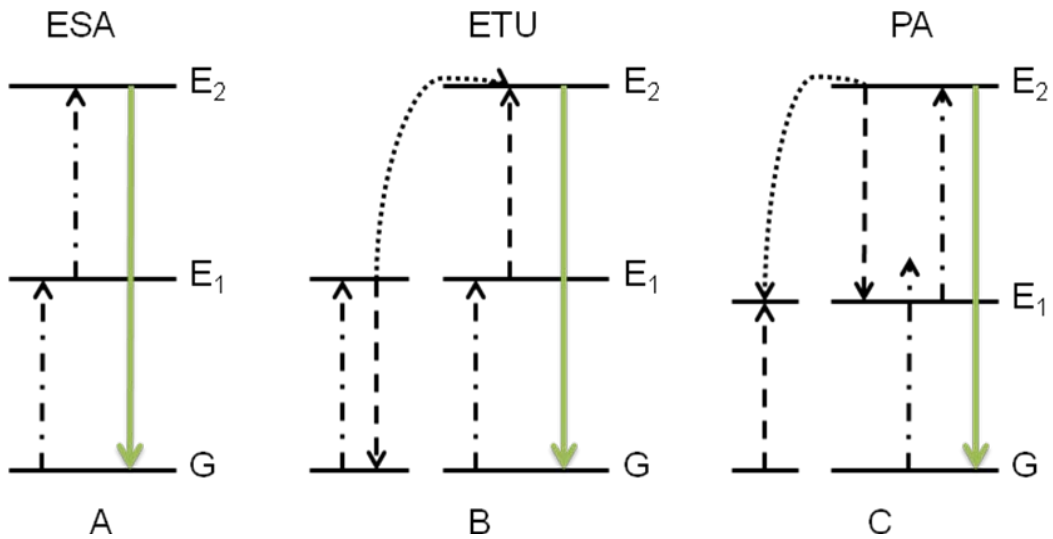
Figure 1.1 The three main UC process in RE doped materials. (A) ESA (excited state absorption) process, (B) ETU (energy transfer up-conversion) process, (C) PA (photon avalanche) process. The dash and dots, dash, and solid lines indicate the excitation, energy transfer, and emission process respectively. (The dots curve shows the direction of the energy transfer process.)
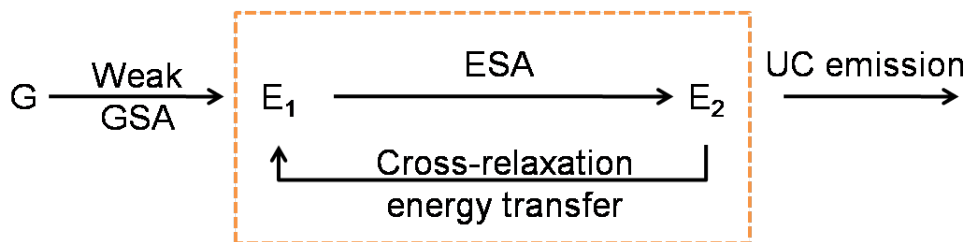
Figure 1.2 Illustration of the PA (photon avalanche) process; G (ground state), GSA (ground state absorption), E_1 (first excited state), E_2 (second excited state), ESA (excited state absorption).

1.1.2 Example of the ETU up-conversion process

Among the three up-conversion processes, ETU has a higher efficiency than ESA [2], which does not require a threshold pump intensity as PA. Consequently, it shows better potential applications such as bio-probe [2, 3]. Yb-Er ,Yb-Tm and Yb-Ho co-dopants demonstrate the typical ETU process and have been reported to show the highest UC efficiencies up-to-date [2, 3]. Based on the spectra and energy levels of rare earth ions in crystals [5], the detailed energy transfer mechanism is illustrated in **Figure 1.3**. Yb^{3+} has only one excited 4f level $^2F_{5/2}$ which has a larger absorption cross-section and much higher concentration quenching limit than that of other lanthanide ions [2]. Consequently, Yb^{3+} is normally used as sensitizer with high doping concentration (~ 20 mol%). The $^2F_{7/2}$ - $^2F_{5/2}$ transition of Yb^{3+} is resonant with many ladder-like arranged energy levels of lanthanide ions (such as Er^{3+} in **Figure 1.3**, acting as activators to emit light) resulting in high UC efficiency. After undergoing different non-radiative processes, the excited ions can finally produce red, green and blue emissions. (A detail discussion on the up-conversion process of CaF_2:Yb,Er can be found in chapter 4).
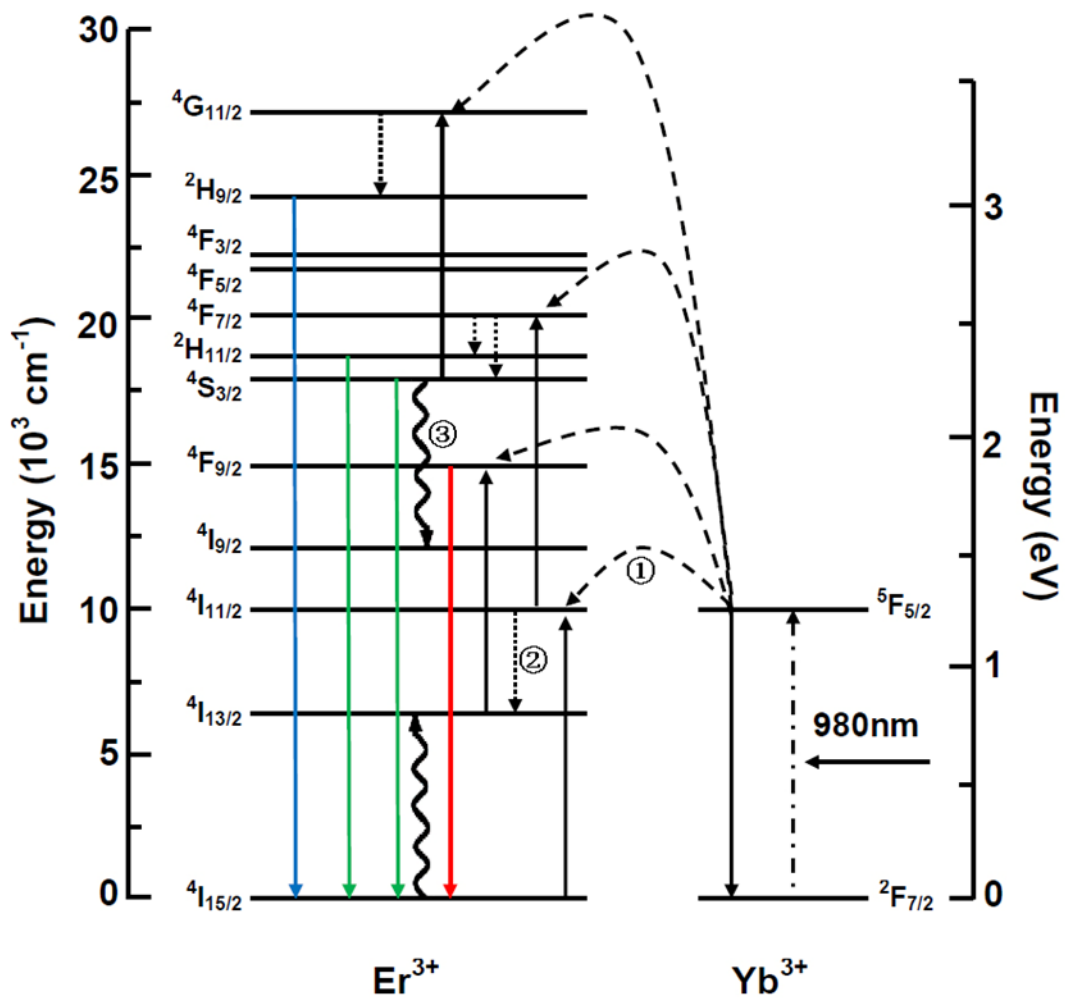
Figure 1.3 UC processes in Er^{3+} and Yb^{3+} doped crystals under 980-nm diode laser excitation. The dashed-dotted, dashed, dotted, and full arrows represent excitation, energy transfer, multi-phonon relaxation, and emission processes, respectively. The pair of arrows with curve shows the cross-relaxation process. Only visible and NIR emissions are shown here.

1.2 Up-conversion efficiency

One key parameter of the UC process is the up-conversion efficiency. The efficiency of luminescence emission can be considered on energy or quantum basis. In this thesis, up-conversion efficiency refers to the quantum efficiency, which can be defined as the number of emission photons divided by the incident photons as [4]

$$\eta = \frac{N_e}{N_i}$$

where η refers to the up-conversion quantum efficiency, N_e is the number of emit photons, and N_i is the incident photons. Theoretically, the up-conversion efficiency will not exceed 50% for a 2-photon excitation process. In fact, the up-conversion efficiency is greatly influenced by the non-radiative processes, which can be divided into resonant energy transfer, multi-phonon relaxation, and cross relaxation [2, 3].

When two RE ions are close enough and their energy levels are able to become resonant (**Figure 1.3** ①), the excited ions can transfer its energy to nearby ions without emission. This kind of resonant energy transfer process is utilized to enhance the efficiency of up-conversion process. A typical example is the Yb-Er co-doping system as discussed before. The sensitizer can greatly increase absorption of the incident light, resulting in the enhancement of the total efficiency. This process also depends on the sensitizer/activator ratio.

The most significant non-radiative de-excitation that competes with radiative de-excitation is multi-phonon relaxation. In case of the strong electron-lattice coupling, the excited electron may lose its energy by way of lattice vibration, undergoing a multi-phonon relaxation (**Figure 1.3 ②**). The multi-phonon relaxation rate k_m can be estimate by energy gap law as [2].

where β is empirical constant of the host materials, is the energy gap between the excited state and the lower energy level, and $\hbar\omega_{max}$ is the highest-energy vibration mode of the host lattice.

Cross-relaxation is also a non-radiative process among the RE ions. An excited ion transfers part of its energy to a nearby ion, lowering its energy from the excited state E_4 to E_3 (**Figure 1.3 ③**), whereas the other ion is pumped from E_1 to E_2. The energy gaps of E_3-E_4 and E_1-E_2 should be quite similar. This process may result in change of the population of a certain excited state, and the change of luminescence color.

Concentration quenching can be explained based on the process illustrated in **Figure 1.4**. When the doping concentration is very high, the distance between doping ions become much shorter. Consequently, the energy transfer process,

such as resonant energy transfer or cross-relaxation, will be much more efficient. As a result, the energy can be transferred among a large number of doping ions before emission takes place. Finally, when the energy transfers to poison (contaminations, defects and etc.), it will be lost as heat without emission by undergoing multi-phonon relaxation process.
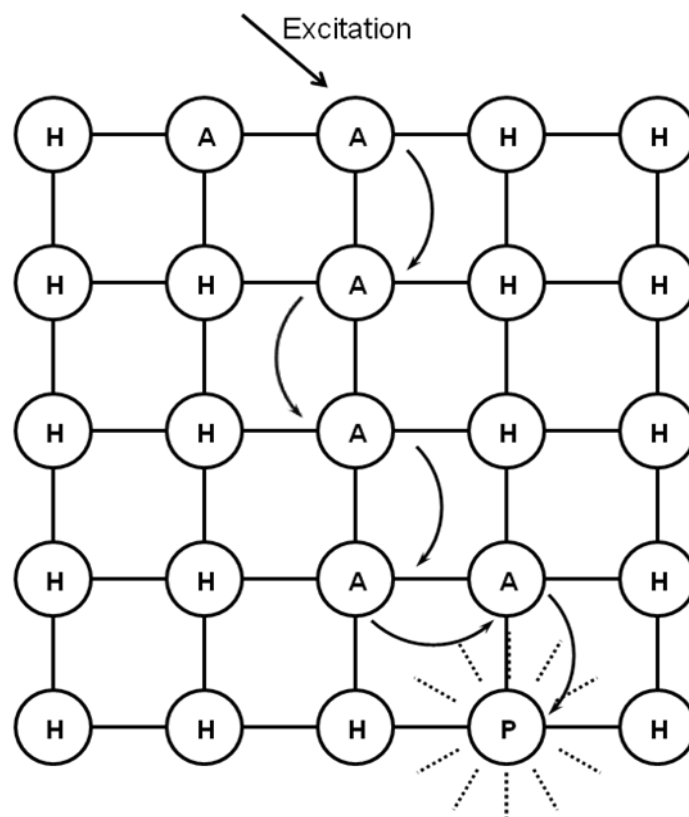
Figure 1.4   Illustration of concentration quenching effect. Host lattice (H), activator (A), poison (P)

1.3 Up-conversion materials

Efficient up-conversion can only be achieved from a few up-conversion materials with combination of certain host and dopants, as illustrated in **Figure**

1.5. The up-conversion materials mainly consist of host materials and dopants, which can be further divided into sensitizer and activator.
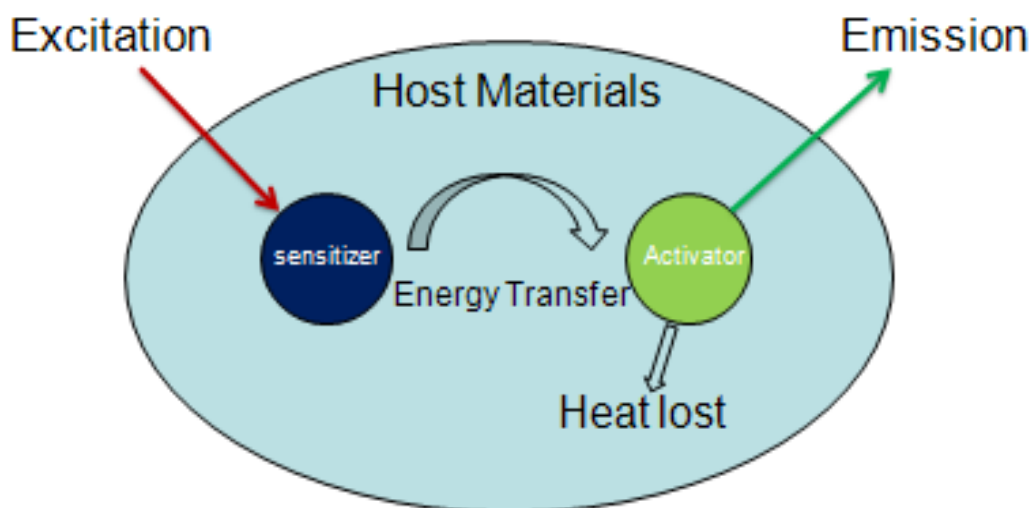
Figure 1.5 Simplified structure of RE co-doped up-conversion materials

1.3.1 Host materials

The oxides and fluorides are often chosen as hosts due to their high optical transparency and low phonon vibration energy, which will minimize the absorption of incident and emission light, and the phonon loss. Although chlorides and bromides show even lower phonon energy than fluorides, they are prone to hygroscopic degradation [6]. To date, the fluoride UC host β-NaYF$_4$ is reported to exhibit the highest UC efficiency [3].

1.3.2   Dopants

As mentioned in Yb-Er up-conversion system, this co-dopants system consists of sensitizer (energy donor), and activator (luminescence emitter).

Most of the RE ions have the ladder-like arranged intermediate energy levels, and exhibit UC properties. Extensive studies have already been conducted on $Pr^{3+}(4f^2)$, $Nd^{3+}(4f^3)$, $Gd^{3+}(4f^4)$, $Dy^{3+}(4f^7)$, $Ho^{3+}(4f^{10})$, $Er^{3+}(4f^{11})$, $Tm^{3+}(4f^{12})$ [2].

In fact, the up-conversion luminescence efficiency is quite low based on this single activator, thus the sensitizer is used to improve the efficiency. Generally, a sensitizer has a single excited level which does not show up-conversion property itself. They should be able to absorb the pumping photons and resonate with the activators. For example, Yb^{3+} ($4f^{14}$) is a typically sensitizer for 980 nm excitation.

Although some transition metal ions also exhibit UC properties, such as $Ti^{2+}(3d^2)$, $Cr^{3+}(3d^3)$, $Ni^{2+}(3d^8)$, $Mn^{2+}(3d^5)$, $Mo^{3+}(4d^3)$, $Re^{4+}(5d^3)$ and $Os^{4+}(5d^4)$, their optical properties change a lot in different host materials due to lack of shielding effect as RE ions [2]. As a result, RE ions are more advantageous in applications and they are the focus of this study.

1.4 Recent synthesis methods for up-conversion nanoparticles

In spite of the unique optical properties of UC materials, their applications have been limited to UV-tuneable laser [4], 3D flat-panel displays [7], infrared quantum counter [1], and temperature sensors [8] in the past few decades. With the development of nanotechnology in recent years, the UC nanoparticles (UCNPs) now can be routinely synthesized (**Table 1.1**).

Table 1.1 Comparison of typical sythesis methods of UC nanocrystals

Method	Advantages	Disadvantages
Co- precipitation	Cheap raw materials and equipment;	Post-annealing often required; vulnerable to aggregation
Sol-gel	Cheap raw materials and equipment	Calcinations required; vulnerable to aggregation
Thermal- decomposition	Small size, narrow size distribution	Expensive precursors; toxic by-products
Solvothermal	Cheap raw materials and equipment; Highly crystalline phase	Potential safety concerns imposed by high pressure and Temperature; unable to observe the process

Yi et al. have first demonstrated the synthesis of $NaYF_4$:Yb,Er up-conversion nano particles using co-precipitation method in the presence of ethylenediaminetetraacetic acid (EDTA) [9] with particle size ranging from 37

to 166 nm. Co-precipitation and sol-gel methods normally require post-deposition that lead to undesired crystal growth, rendering it difficult to obtain nano-size particles. These methods tend to produce particles with a large size distribution.

Using high temperature decomposition method to get $NaYF_4$: Yb,Er up-conversion nano particles was first reported by Heer et al. [10]. The single precursor high temperature decomposition approach to obtain rather uniform LaF_3 nanoparticles was then developed by Zhang and co-workers [11]. The main advantage of this approach is that high quality (small size, narrow size distribution and high crystallinity) nano particles could be produced.

Another frequently used method is solvent-thermal, which was demonstrated by Wang and Li in the synthesis of $NaYF_4$:Yb,Er [12]. A general liquid–solid–solution (LSS) approach to prepare NPs was also reported [13]. This "one pot reaction" method takes advantage of lower reaction temperatures. However, safety may be a concern in this high-pressure reaction carried out in autoclaves. The synthesis of UC nanoparticles has attracted much attention, as can be seen in the literature [9-56]. A summary of part of recent publications can be found in **Table 1.2**.

Table 1.2 Summary of the recently publications of RE doped nano-particles

Year	Ref. NO.	Materials	Method
2004	**[10]**	$NaYF_4$:Yb,Er	Thermal decomposition (CF_3COOH)
2006	**[28]**	$NaYF_4$:Yb,Er	Thermal decomposition (CF_3COOH)
2006	**[51]**	$NaYF_4$:Yb,Er	Co-precipitation (Ethylene glycol+PVP)
2006	**[19]**	$NaYF_4$:Yb,Er	Thermal decomposition (CF_3COOH)
2006	**[55]**	CaF_2:Ce,Tb	Co-precipitation (DEG)
2006	**[54]**	CaF_2:Er & LaF_3:Nd	Co-precipitation (1-4-butanediol & ethylene glycol)
2007	**[29]**	$NaGdF_4$: Ce^{3+}, Tb^{3+}	Thermal decomposition (CF_3COOH)
2007	**[15]**	$NaGdF_4$:Eu^{3+}	Thermal decomposition (HEEDA)
2007	**[42]**	MF_2 (M = Ca, Sr, Ba)	Solvothermal (oleic acid and ethanol)
2008	**[41]**	MF_2 (M = Ca, Sr, Ba)	Thermal decomposition (CF_3COOH)
2008	**[17]**	KYF_4:Yb,Er	Thermal decomposition (HEEDA)
2008	**[44]**	$NaYF_4$:Yb,Er,Tm	Solvothermal (PEI)
2008	**[53]**	$NaYF_4$:Yb,Er,Tm	Solvothermal (oleyacid &1-octadecene)
2009	**[50]**	BaF_2:Eu^{3+}	Solvothermal (oleic acid & alcohol)
2009	**[38]**	SrF_2 : Eu^{3+}	Microemulsion-mediated Solvanthermal
2009	**[46]**	MF_2 (M = Ca, Sr, Ba)	Thermal decomposition (CF_3COOH)
2009	**[34]**	KY_3F_{10}:Yb,Er &Eu	Thermal decomposition (CF_3COOH)
2009	**[33]**	$NaGdF_4$:Ho^{3+}/Yb^{3+}	Thermal decomposition (CF_3COOH)
2009	**[35]**	$BaYF_5$:Tm^{3+}, Yb^{3+}	Thermal decomposition (CF_3COOH)
2009	**[27]**	$NaYF_4$:Yb,Er(Tm)	Thermal decomposition (OA & ODE)
2009	**[39]**	CeF_3:Tb^{3+}	Solvothermal (trisodium citrate)
2009	**[43]**	$KMgF_3$:Tb^{3+}	Microwave Irradiation decomposition
2010	**[56]**	$NaYF_4$:Yb,Er nanorod	Solvothermal

1.5 Applications of up-conversion nanoparticles

Most of the applications of UCNPs utilize the unique optical properties, such as NIR low photon energy excitation source and sharp emission lines.

Bio-applications

Organic dyes are one of the commonly used bio-labeller, however, their photo stability is too low for long-duration imaging. Although QDs are more resistant to photo bleaching compared with organic dyes, they both suffer from low signal-to-noise ratio problem due to the use of UV excitations that cause undesired auto-fluorescence from bio-molecules [3, 19]. More recently, the lanthanide-doped UC nanocrystalls have drawn lots of interests on bio-application.

For example, UCNPs for bio-imaging was reported by Lim et al. [57]. They synthesized Y_2O_3:Yb/Er NPs ranging from 50–150 nm and inoculated these nanoparticles into live nematode. The digestive system of the worms could be clearly imaged upon excitation at 980 nm laser, based on the statistical distribution of the nanoparticles. Li et al incubated silica coated $NaYF_4$:Yb,Er nanospheres in physiological conditions with Michigan Cancer Foundation - 7 cells [52]. Fluorescence from the nanospheres was observed in the cells with high signal-to-background ratio using a confocal microscope under 980nm

NIR laser excitation

The UCNPs have also been used as biosensor to detect biomolecules (DNA and protein), pH value, etc. Wang and co-workers adopted gold NPs as the energy acceptors [58]. Using the specific interaction between avidin and biotin, the aggregation of UCNPs and gold NPs could be triggered to realize the fluorescence resonance energy transfer (FRET) process to detect DNA. A detection limit of 0.5 nM for avidin was demonstrated based on this method. Another example of using FRET to detect DNA was reported by Zhang et al. [59]. Instead of gold, they have used fluorophore (carboxytetramethyl-rhodamine) as the energy acceptor and the detection limit was 1.3 nM for 26-base oligonucleotide. The first optical pH sensor based on upconversion luminescence was demonstrated by Wolfbeis et al [60], which may be refined to measure the pH in deeper regions of tissue.

Solar Cell Application

The conventional silicon single crystal solar cell only absorbs wavelengths shorter than 1100 nm, corresponding to its band gap energy of ~ 1.12 eV. The Air Mass (AM) 1.5 terrestrial solar spectra wavelengths range from 200 nm to 2500 nm [61], covering the UV, visible and IR light. None of the currently available solar cells is able to utilize all of the energy of these wavelengths.

This problem has been approached by coating an up-converter layer on solar cells to improve the total efficiency. Shalav et al. [61] applied the NaYF$_4$:Er^{3+} UC material to a bifacial silicon solar cell. This work demonstrated that photons with wavelengths above 1100 nm could be converted to electricity by a silicon solar cell with the aid of an up-converter. The theoretical calculation on the maximum conversion efficiency after coating with a up-converter layer was studied by Trupke et al. [62]. The maximum efficiencies were estimated to be 50.7% and 40.2% for materials with bandgap of 2.0 eV and 1.12 eV respectively, suggesting the potential for UCNPs to enhance solar cell efficiency

Chapter 2

2 Research Motivation and Experiment Design

2.1 Research Motivation

Recently, the nano-sized luminescence materials have attracted increasing attention as ultrasensitive fluorescent bio-probes for analytical and biophysical applications [3, 9, 63-65]. Among them, the rare earth (RE)-doped up-conversion nano particles (UCNPs) have been attracting significant interests [9, 10, 19, 28].

Traditional down-conversion luminescent materials, such as organic dyes, semiconductor nanocrystals (quantum dots, QDs) [64] and florescence proteins [63, 66], suffer from low signal-to-noise ratio problem due to the use of UV excitations that cause undesirable auto-fluorescence from biomolecules [3]. As the NIR excitation lies in the optical window of human body (650 - 1200 nm), UCNPs benefit from a deeper penetration depth. As the photon energy of NIR excitation source is much lower compared with that of UV, background auto -fluorescence, photo bleaching and photo damage to biological specimens have been largely minimized [3, 19]. In addition, UCNPs consist of

much less toxic elements compared with that of QDs. The use of inexpensive 980 nm NIR laser as pumping source adds another advantage to the use of these UCNPs. As a result, the UCNPs show great potential in bio-application

Obviously, the synthesis of UCNPs with well-controlled, optimized properties is fundamental to its applications. However, most of the current works are based on $NaYF_4$:Yb,Er whereas other up-conversion nanoparticles have not as well explored. For example, CaF_2 has low effective phonon energy (~ 280 cm^{-1}) [54], that minimizes the non-radiative loss. It also has large optical transparency (~ 0.15 μm to 9 μm), which will minimize the absorption of incident and emission light. Both features make it suitable for up-conversion host materials. It is an agent for bone/teeth reconstruction, and has been demonstrated to have good biocompatibility [55, 67].

In this thesis, the synthesis and characterization of CaF_2:Yb,Er and CaF_2:Yb,Er(core)/CaF_2(shell) were carried out. The comparison of different size of CaF_2:Yb,Er(core)/CaF_2(shell) and CaF_2(core)/CaF_2:Yb,Er(shell) were conducted**.** Silica coating on the UCNPs was also achieved to demonstrate its potential for bio-application.

2.2 Experiment Design

2.2.1   Host materials selection

Calcium fluoride (CaF_2) is considered to be one of the best optical materials for its large regions of transparency (about 0.15 µm to 9 µm). It finds its application in window materials as well as the host materials for laser application [68]. Plenty of work has been done on bulk CaF_2 materials.

Recently, the sub-micron and nano-sized CaF_2 materials have attracted increasing attention. Li et al have reported the synthesis of size-controlled CaF_2 nanocubes using a hydrothermal method in the absence of surfactants, with the average particles size ~ 350 nm [69], Feldmann et al used a polyol-mediated method to get nanoscale CaF_2 at ~ 20 nm [55]. The synthesis of the series of nano-sized alkaline earth metal fluorides (MF_2, M = Ca, Sr, Ba) has also been reported [41, 42]. However, all these nano-size CaF_2 nanoparticles were used for down-conversion luminescence host materials. Very recently, Li et al demonstrated the up-conversion optical property of CaF_2:Yb,Er [49]. In this thesis, the synthesis of nanoscale CaF_2:Yb,Er was investigated. The core/shell structure was studied to optimize the up-conversion optical properties.

2.2.2   Dopants selection

Yb^{3+} is normally used as sensitizer with high doping concentration due to its high concentration quenching limit and large cross-section. Yb-Er, Yb-Ho and Yb-Tm are three normally used co-dopants, showing much higher up-conversion efficiency compared with single doped systems such as Er, Ho and Tm. Among them, Yb-Er is the most efficient up-conversion doping pair reported so far [2]. The ion size of Ca^{2+}(114pm), Yb^{3+}(101pm), Er^{3+}(103pm) are quite similar, which will facilitate the doping process [70]. Therefore, Yb-Er co-dopants were chosen in this study.

2.2.3   Core shell structure

The core-shell structure had been previously reported in QDs, such as CdSe/CdS, CdSe/ZnS [71-73]. ZnS, which is normally used as the shell layer, has a larger band-gap than that of core. It does not create intermediate energy levels within the original band-gap. Instead, it can passivate the core, prevent leaking of toxic ions, protect core from oxidation and improve the quantum efficiency as the same time.

The core/shell structure has also been applied in the RE doped UCNPs system [20]. Chow et al. reported a 7-times and 29-times enhancement of total intensity after coating undoped NaYF$_4$ on NaYF$_4$:Yb,Er and NaYF$_4$:Yb,Tm

respectively [20]. By coating an undoped shell, the total intensity improved from several times to tens of times in different UCNPs systems [20, 36, 53].

Based on the previously reported method for preparing core/shell (C/S) UC nanoparticles of NaYF$_4$:Yb,Er [20], CaF$_2$:Yb,Er core and CaF$_2$:Yb,Er/CaF$_2$ core/shell (C/S) nanoparticles were investigated.

Chapter 3

3 Synthesis and Characterization of CaF$_2$:Yb,Er nanoparticles

3.1 Introduction

In the past few years, controlled synthesis of nanostructures has attracted much interest and the nanostructures are readily available as 0D, 1D, and 2D [13, 65, 74-76]. Taking bio-probe application for example, the luminescent NPs should be small enough ($\leqslant$ 10 nm) with a narrow size distribution in order to mark the targets such as oligonucleotides, proteins and other biomolecules ranging from several nanometers to tens of nanometers [19].

In this chapter, the thermal decomposition method was used to prepare high quality (small size, narrow size distribution and high crystalline) CaF$_2$:Yb,Er NPs. The as-synthesised CaF$_2$:Yb,Er NPs were then characterized by XRD, TEM, FTIR.

3.2 Method

3.2.1 Chemicals

Oleylamine (CH$_3$(CH$_2$)$_7$CH=CH(CH$_2$)$_8$NH$_2$, 70%), ytterbium chloride

hexahydrate (YbCl$_3$·6H$_2$O, 99.99%), erbium chloride hexahydrate (ErCl$_3$·6H$_2$O, 99.99%), and trifluoroacetic acid(CF$_3$COOH >98%) were obtained from Sigma-Aldrich (Sigma-Aldrich, Singapore). Ammonia solution (NH$_3$·nH$_2$O, 28%) was purchased from APS Fine Chem. Calcium carbonate (CaCO$_3$) was ordered from Acros Organics. Argon was obtained from SOXAL (Ar, 99.995%). Ultra pure water (18.0 MV) from a Milli-Q deionization unit was used throughout the experiment. Rare earth chloride stock solutions with a concentration of 0.2 M were prepared by dissolving YbCl$_3$·6H$_2$O and ErCl$_3$·6H$_2$O in de-ionized water. The final solutions were adjusted to pH = 2 to avoid hydrolysis.

3.2.2 Equipment

A JEOL TEM 2010 (JEOL, Japan) transmission electron microscope was operated at 200 kV. Samples were prepared by sonicating 1 mg precipitates in 1 mL hexane, and a drop of the suspension was put onto a formvar/carbon film supported TEM Cu grid. Powder X-ray diffraction (XRD) spectra were acquired with a D8 advance X-ray diffractmeter, with Cu K$_\alpha$ radiation at 1.5406 Å, using a step size of 0.02 $^{\circ}$ and a count time of 0.2 s. Thermo gravimetric analysis (TGA) and differential thermal analysis (DTA) were used to study the thermal behavior of precursors by using a thermogravimetric analyzer (SDT Q600). 13.535 mg of powders were

investigated using a heating rate of 10 °C/min in a nitrogen flow of 70 mL/min. Fourier transform infrared (FTIR) spectra were measured using a Varian FT3100 spectrometer (Palo Alto, CA). 1 mg of precipitates was re-dispersed in hexane and then deposited on a KBr pellet.

3.2.3   Precursor preparing

The rare earth chlorides were precipitated in excess ammonia, centrifuged and then washed 5 times in de-ionized water.   Rare earth trifluoroacetates $((CF_3COO)_3RE)$ were prepared by dissolving respective rare earth hydroxides in trifluoroacetic acid(CF_3COOH), followed by drying in an oven at 80 ^{o}C. Calcium trifluoroacetate $((CF_3COO)_2Ca)$ were prepared by dissolving calcium carbonate $(CaCO_3)$ into trifluoroacetic acid.

3.2.4   Synthesis CaF₂: Yb, Er Nanoparticles

The synthesis of CaF₂:Yb,Er nanoparticles was modified based on the previous reported high-temperature-decomposition method [20]. In a typical procedure (**Figure 3.1**) for the preparation of CaF₂:Yb,Er nanocrystals, a mixture of $CF_3COO)_2Ca$ (0.78 mmol), $(CF_3COO)_3Yb$ (0.2 mmol), and
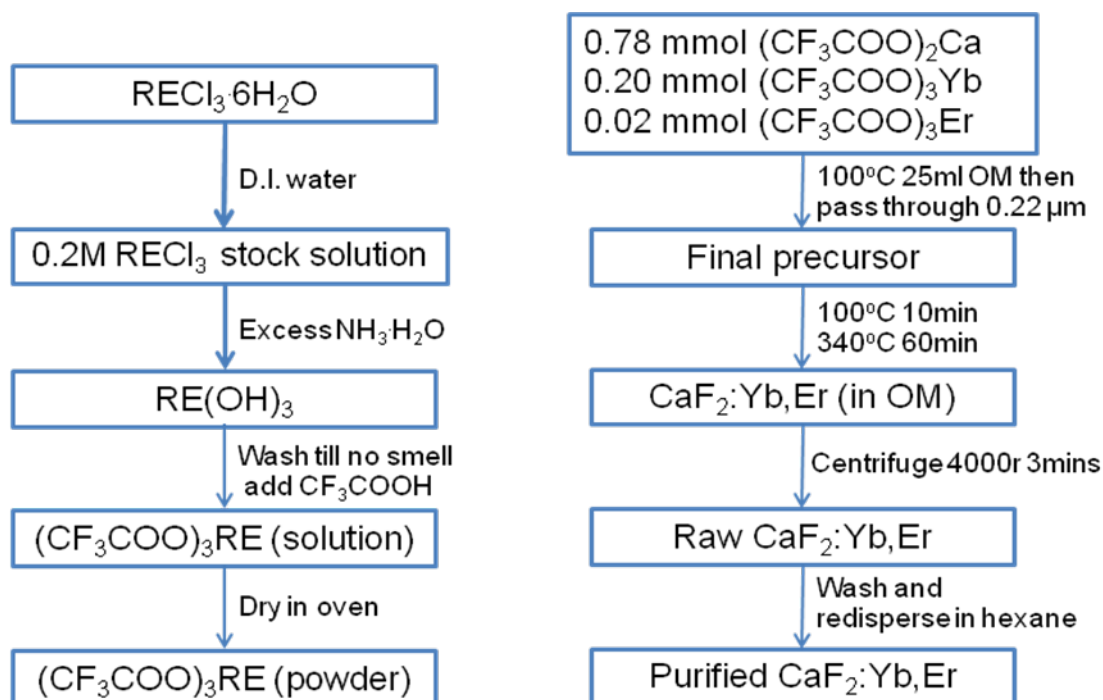
Figure 3.1 A flow chart for the preparation of CaF$_2$:Yb,Er NPs

(CF$_3$COO)$_3$Er (0.02 mmol) was dissolved in oleylamine (OM) (25 mL), then passed through a 0.22 µm filter (Millipore) to remove any residues. Under vigorous stirring in a 50 mL flask, the mixture was heated in argon to 100 °C and kept for 10 min, then the temperature was increased to 340 °C at the rate of 10 °C/min (the setup of thermal-decomposition synthesis is show in **Figure 3.2**). The reaction was maintained at 340 °C for 1 h.   A transparent yellow solution was obtained. As-synthesized nanoparticles were isolated by centrifugation and subsequently dispersed in hexane. The surfactants on these particles could be removed by washing in excess ethanol.

Thermocouple

Heating Mantle

Stirrer

Ar
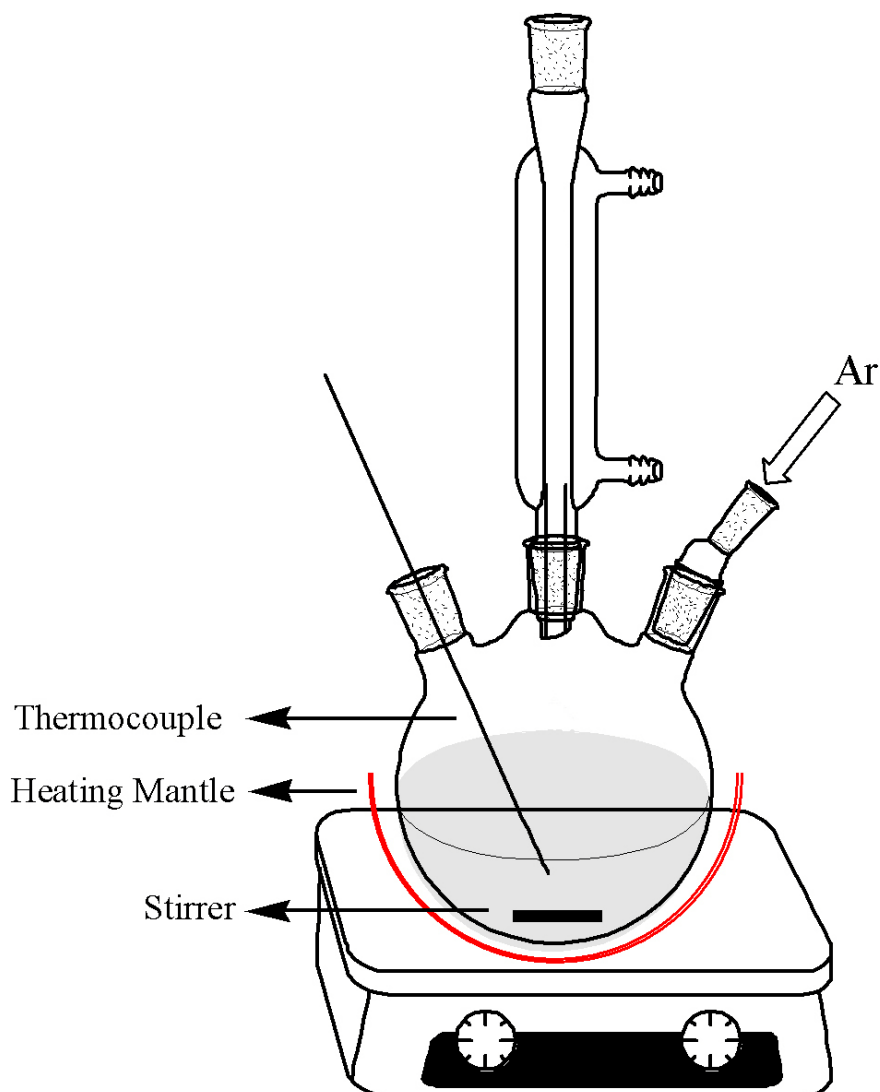
Figure 3.2 The reaction setup of thermal-decomposition synthesis of CaF$_2$

3.3 Results and Discussion

3.3.1 Structure

Figure 3.3 shows the XRD spectra of the CaF$_2$:Yb,Er nanocrystals and the

vertical bars below are from the corresponding standard card
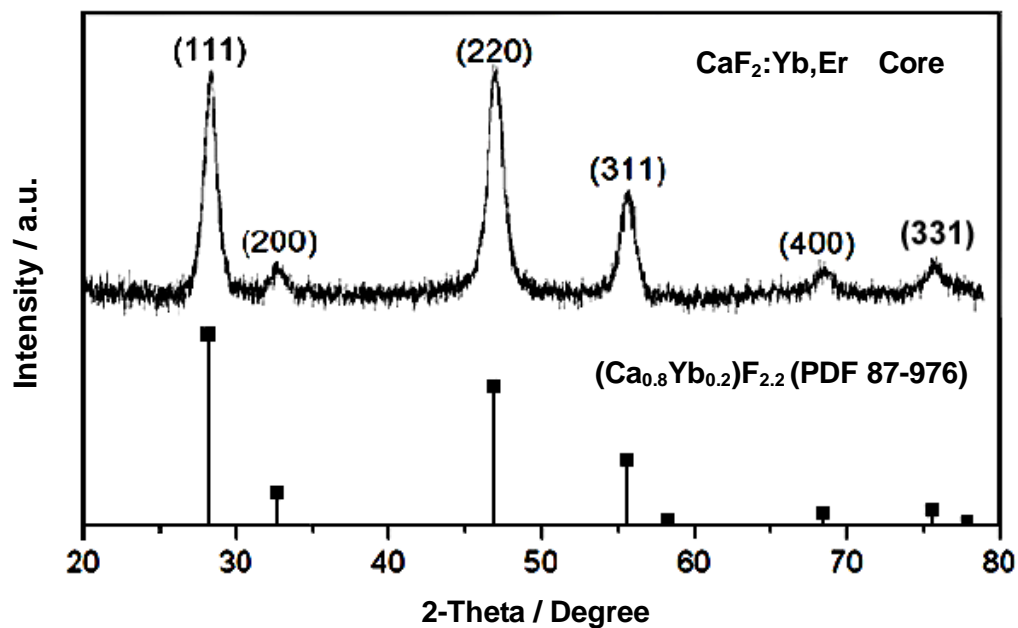
Figure 3.3 X-Ray powder diffraction pattern of as-synthesized CaF$_2$:Yb,Er nanoparticles and standard reference (Ca$_{0.8}$Yb$_{0.2}$)F$_{2.2}$ (PDF 87-976)

(Ca$_{0.8}$Yb$_{0.2}$)F$_{2.2}$ (Joint Committee on Powder Diffraction Standards (JCPDS) file number PDF 87-0976). The X-ray peak positions and intensities of the nanocrystals generally matched well with the reference (Ca$_{0.8}$Yb$_{0.2}$)F$_{2.2}$ (PDF 87-0976). For pure CaF$_2$, the (200) peak had a negligible intensity, corresponding to an allowed X-ray diffraction of the fluorite-type [77]. As Ca^{2+} and RE^{3+} have close ionic sizes [3], RE^{3+} doping ions substitute the Ca^{2+} site, with extra F$^-$ ions going into interstitial sites to compensate the extra charge [41, 78]. The intensity of the (200) diffraction peak increased because of the different atomic number between the RE and Ca, especially at a high doping level [77]. As reported in the literature, the appearance of (200) peak in the RE^{3+} doped CaF$_2$ is a signature of incorporation of RE^{3+} in CaF$_2$ host [79, 80], confirming the successful doping of Yb^{3+} and Er^{3+} ions

into the CaF$_2$ host. The (220) peak of as-synthesized sample showed a higher intensity compared with the reference, indicating a possible slight texturing. Note that in the reference standard (PDF 87-976) only included 20% doping, but not the Er doping. The 2% Er doping in our study here would not be expected to have significant influence on the general features of reference standard (PDF 87-976)

The X-ray peak broadening was used to estimate the average crystallite using Scherer's equation.

$$D_{hkl} = K\lambda/(\beta \cos\theta)$$

where D$_{hkl}$ means the size along the (hkl) direction, K is a constant (0.89), λ is the wavelength of X-ray that was used (0.15406 nm), β is the full width at half-maximum, and θ is the diffraction angle. The average crystallite size was estimated as ~ 6 nm

3.3.3 Morphology

Figure 3.4 shows a typical TEM bright field image of the CaF$_2$:Yb,Er nanocrystals and the inset is the corresponding HRTEM for a single nanoparticle. As-synthesized nanoparticles were quite uniform in size and morphology. The average size of as-synthesized particles, estimated from measuring 100 particles, was 5.4 nm ± 0.9 nm and equiaxed in shape. The

particles size obtained by TEM matched well with the average X-ray crystallite size estimated using Scherer's equation, confirming the particles to be single crystals.
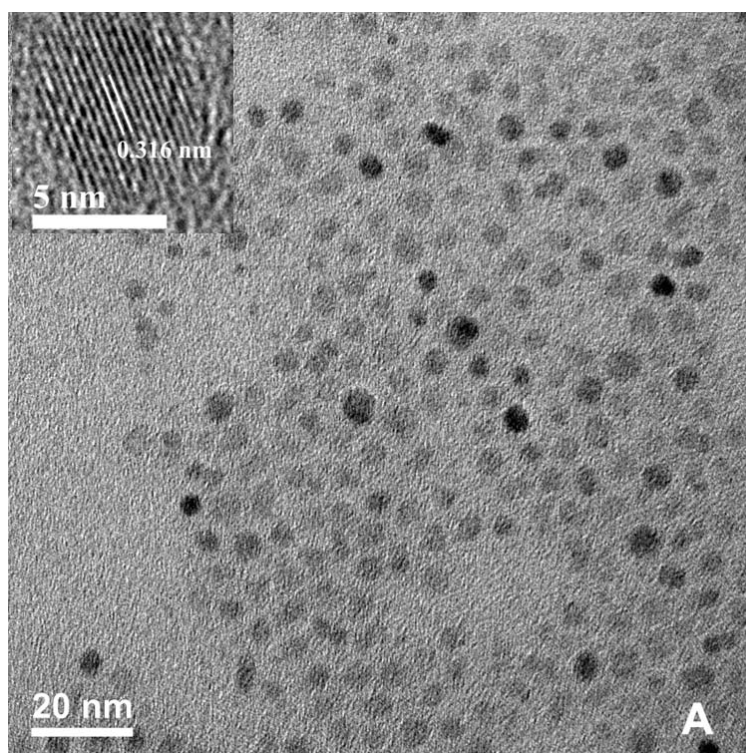
Figure 3.4 TEM bright field image of CaF$_2$:Yb,Er core. Inset is the HRTEM result of CaF$_2$:Yb,Er core

A corresponding HRTEM image of CaF$_2$:Yb,Er is shown in inset of **Figure 3.4** near Scherzer defocus. The distance between the two nearby lattice fringes (~ 0.315 nm) corresponded to the (111) d-spacing of (Ca$_{0.8}$Yb$_{0.2}$)F$_{2.2}$ (PDF 87-0976). As the CaF$_2$:Yb,Er UCNPs are mainly consisted of light element of Ca and F (relative atomic mass are 40 and 17, respectively), it was difficult to obtain a high contrast HRTEM image. In addition, the

random speckled background due to the amorphous carbon substrate could be significant compared with the low contrast sample materials, rendering it harder to get a good quality TEM image for CaF$_2$:Yb,Er. The selected area electron diffraction (SAED) pattern of as-synthesized doped UC nanocrystals is shown in **Figure 3.5.** The ring patterns were caused by the randomly orientated nanoparticles.
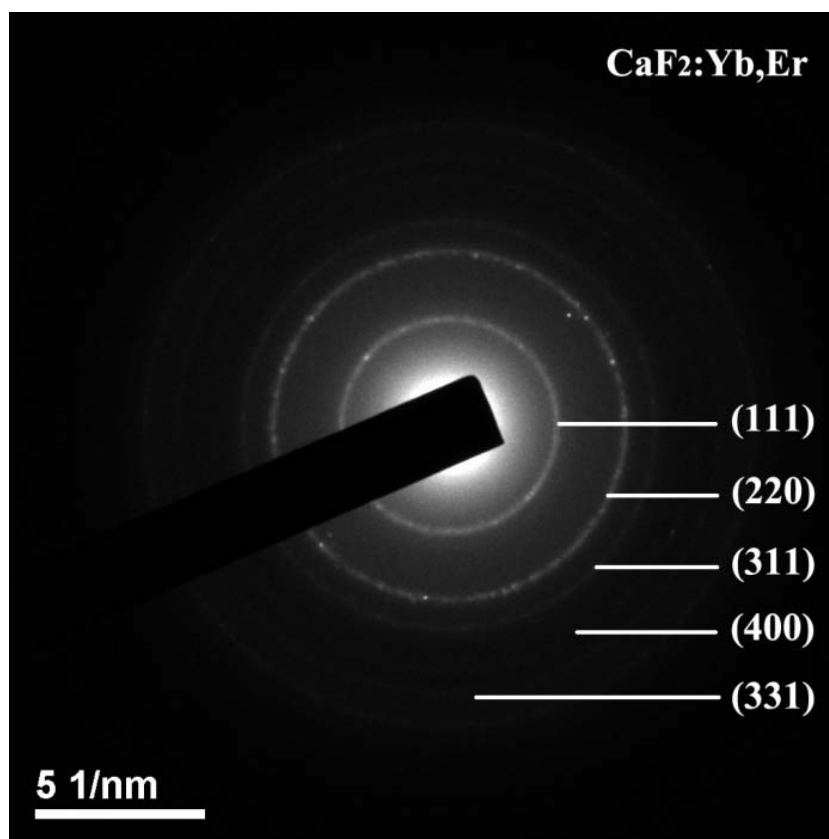
Figure 3.5 Selected Area Electron Diffraction (SAED) pattern of CaF$_2$:Yb,Er core.

3.3.4 DTA/TGA analyze

Figure 3.6 illustrates the weight loss and heat flow of the (CF$_3$COO)$_2$Ca during thermal decomposition. The biggest weight loss occurred in the 300 - 350 °C rang.e, with the exothermic peak at 343 ^{o}C, which was similar to the previously reported decomposition of (CF$_3$COO)$_3$RE [81].
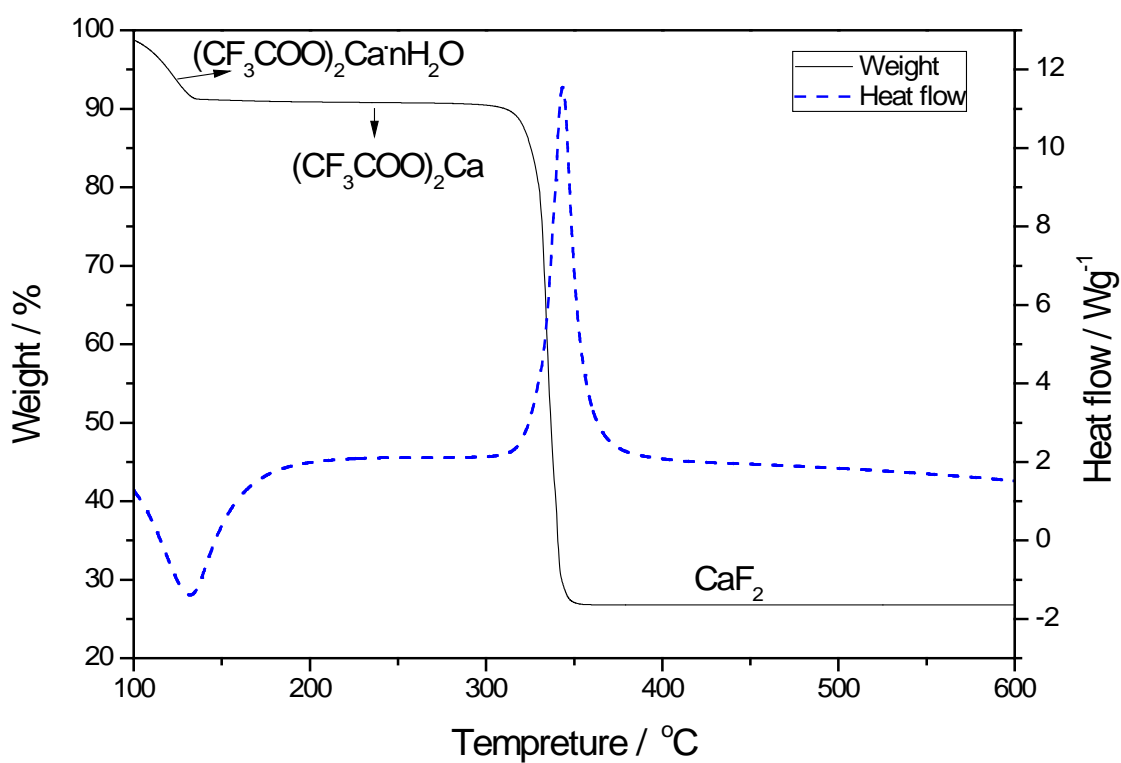
Figure 3.6 Weight loss and heat flow curve of the precursor (CF$_3$COO)$_2$Ca

The exothermic peak corresponded to the decomposition of the $(CF_3COO)_2Ca$, forming the CaF_2 nanocrystals. It is consistent with the observed bubbles formation during the reaction (**Figure 3.7**). At around 340 °C, the sudden increase in the concentration of nanocrystals (burst of nucleation) was followed by rapid narrowing of the size distribution (size focusing) [82], which played a key role to produce high quality nanocrystals.

$$(CF_3COO)_2Ca \rightarrow CaF_2\downarrow + C_2F_4\uparrow + 2CO_2\uparrow$$

Figure 3.7 Chemical reaction formula of high temperature decompose process of $(CF_3COO)_2Ca$ [41]

3.3.5 FTIR results

Figure 3.8 shows the FTIR spectra of CaF_2 precursor, $(CF_3COO)_2Ca$. The sharp peaks located at 1680 cm^{-1}, 1457 cm^{-1}, 1207 cm^{-1} and 1150 cm^{-1} were attributed to the characteristic absorption peak of C=O, C-O and C-F, respectively, confirming the existence of $(CF_3COO)_2Ca$ precursor (summarized in **Table 3.1**).
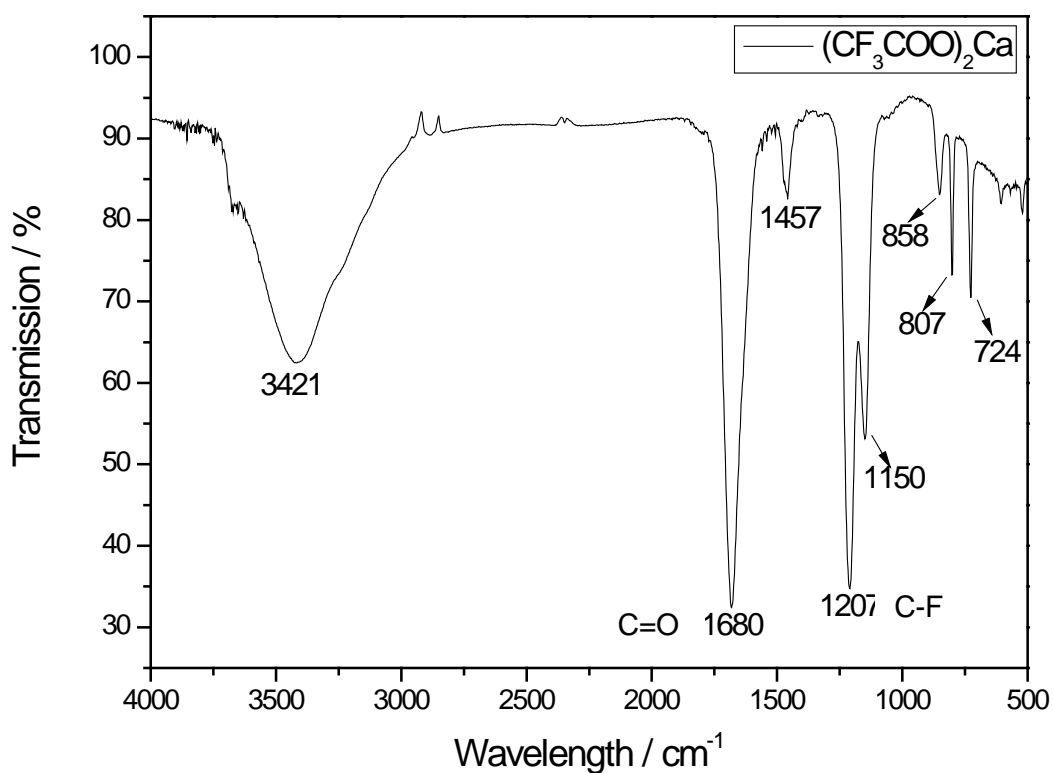
Figure 3.8 FTIR spectra curve of precursor (CF$_3$COO)$_2$Ca

Table 3.1 The FTIR peaks assignment for precursor (CF$_3$COO)$_2$Ca

Wavenumber (cm^{-1})	Assignment
3421	stretch vibration of O-H (may come from excess CF$_3$COOH and water)
1680	stretch vibration of C=O
1457	stretch vibration of C-O
1207, 1150	stretch vibration of C-F

After the decomposition process, as-synthesized nanoparticles were collected, washed and dried before the FTIR test. The characteristic peaks of (CF$_3$COO)$_2$Ca disappeared and new absorption peaks were found (see **Figure 3.9**). The peaks at 3321 cm^{-1} and 1577 cm^{-1} were ascribed to the asymmetric stretching vibration and scissoring vibration of NH$_2$ respectively. The presence of CH=CH group was suggested by the peaks at 1615 cm^{-1} and 3006 cm^{-1}, which were assigned to the stretching vibrations of C=C and =C-H. The peak at 721 cm^{-1} was assigned to the in-planar swing of (CH$_2$)n (n > 4). The sharp peaks at 2852 cm^{-1} and 2922 cm^{-1} were assigned to the symmetric and antisymmetric stretching vibration of the -CH$_2$ group (summarized in **Table 3.2**). These results suggested that the precursor (CF$_3$COO)$_2$Ca was deposited at high temperature to form CaF$_2$ nanoparticles that were capped with oleylamine. The surface capping with oleyamine was a key factor for getting the high quality of UCNPs and making it re-dispersible in solvent such as hexane or chloroform (**Figure 3.10**) [41].
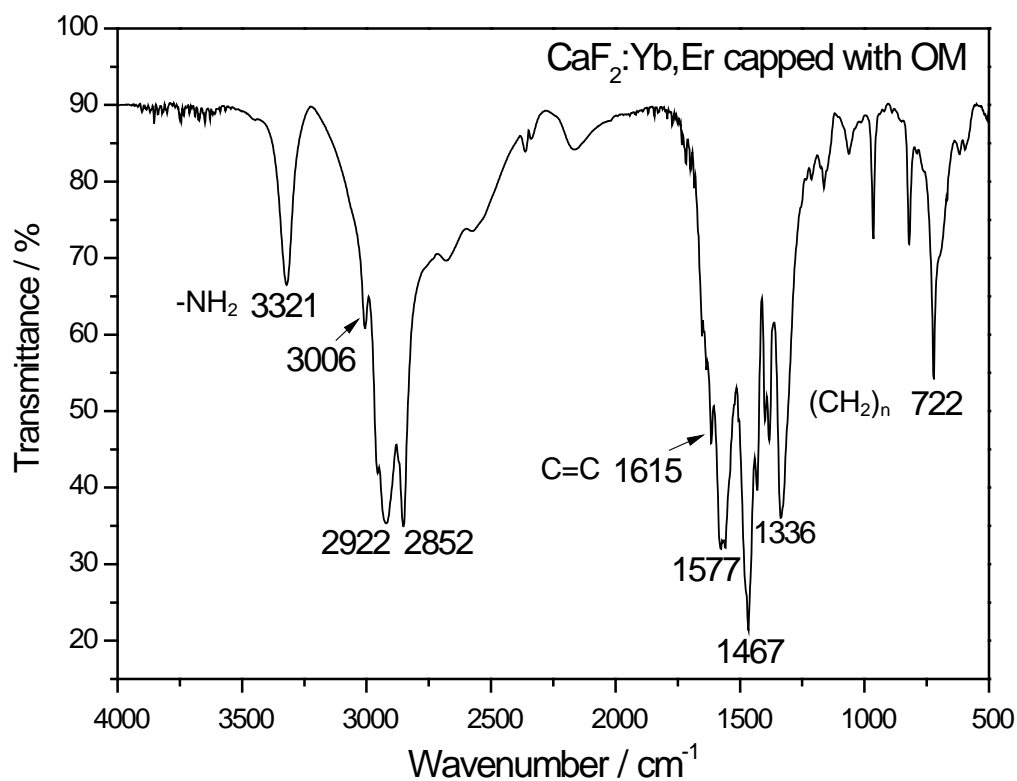
Figure 3.9 FTIR spectra curve of as prepared the OM (oleylamine, CH$_3$(CH$_2$)$_7$CH=CH(CH$_2$)$_8$NH$_2$) capped CaF$_2$ nanocrystals

Table 3.2 The FTIR peaks assignment for OM capped CaF$_2$

Wavenumber (cm^{-1})	Assignment
3321	N-H asymmetric stretching vibration
1577	N-H scissoring vibration
1615	stretching vibrations of C=C
3006	stretching vibrations of =C-H
722	in-planar swing (CH$_2$)n (n > 4).
2852	symmetric stretching vibration of the -CH$_2$
2922	antisymmetric stretching vibration of the -CH$_2$
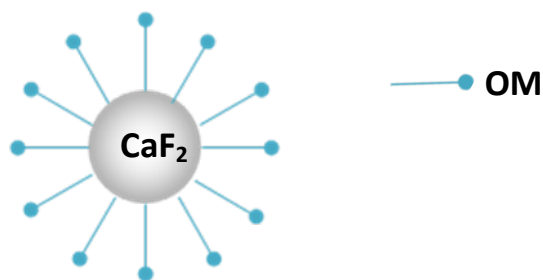
Figure 3.10 A schematic of the OM (oleylamine) capped and stabilized CaF_2 NPs

3.4 Summary

CaF_2:Yb,Er UCNPs were successfully synthesised using thermal-decomposition method at 340 $^{\circ}$C. Estimated from measuring 100 particles, the average size of as-synthesized particles was determined to be ~ 5.4 nm ± 0.9 nm. They were equiaxed in shape with fairly uniform size. Using Scherer's equation, the average crystallite size was estimated as ~ 6 nm. The TEM result indicated that the particles were single crystals. The surfactant OM played a key role to get the high quality NPs, which capped as-synthesised NPs to prevent them from further growth or agglomeration.

Chapter 4

4 Emission enhancement and critical shell thickness of CaF$_2$:Yb,Er(core)/CaF$_2$(shell) nanoparticles

4.1 Introduction

Core/shell structure has previously been applied in the QDs to prevent its oxidation, emitting toxic elements and to improve the total efficiency [64, 73, 83]. One of the best available QD were made of CdSe cores over coated with a layer of ZnS [71, 72, 83]. The ZnS has a larger band-gap than that of CdSe, so it will not create an intermediate energy level but passivate the surface state of CdSe in order to enhance the emission intensity. ZnS has a similar lattice parameter to that of CdSe, thus the epitaxial growth of the shell will be facilitated. In addition, ZnS has a relatively improved chemical and photon stability, so the stability will be improved [64].

Although the main purpose of core/shell structure is to improve the emission intensity for both QDs and UCNPs, the principles are not exactly the same because of their different optical properties. For UCNPs, the optical property is mainly determined by the 4f energy level of the RE ions. As the 4f electrons of

RE^{3+} is shielded by the completely filled $5s^2$ and $5p^6$ orbitals, quantum confinement effects on electronic states of these highly localized electrons around the nucleus are not expected as it is in QDs [84]. As a result, when choosing the coating materials for UCNPs, the main concerns are the phonon energy and lattice parameter of shell materials. The phonon energy of shell materials should be low to minimize the multi-phonon relaxation. The shell materials should also have a similar lattice parameter in order to facilitate the epitaxial growth of shell on the core.

The undoped host materials CaF_2 itself can fulfill the requirements of being the shell materials. It is quite stable, has similar lattice parameter as that of CaF_2:Yb,Er (< 0.2 %) and low phonon energy(~ 280 cm^{-1}) [54]. Using CaF_2:Yb,Er as the seed, an epitaxial growth of the CaF_2 to form CaF_2:Yb,Er(core)/CaF_2(shell) was investigated.

4.2 Method

4.2.1 Chemicals

Oleylamine ($CH_3(CH_2)_7CH=CH(CH_2)_8NH_2$, 70%), ytterbium chloride hexahydrate ($YbCl_3 \cdot 6H_2O$, 99.99%), erbium chloride hexahydrate ($ErCl_3 \cdot 6H_2O$, 99.99%), and trifluoroacetic acid, (CF_3COOH >98%) were obtained from Sigma-Aldrich (Sigma-Aldrich, Singapore). Ammonia solution ($NH_3 \cdot nH_2O$, 28%)

was purchased from APS Fine Chem. Calcium carbonate ($CaCO_3$) was ordered from Acros Organics. Argon is obtained from SOXAL (Ar, 99.995%). Ultra pure water (18.0 MV) from a Milli-Q deionization unit was used throughout the experiment. Rare earth chloride stock solutions with a concentration of 0.2 M were prepared by dissolving $YbCl_3 \cdot 6H_2O$, $ErCl_3 \cdot 6H_2O$ respectively in de-ionized water. The final solutions were adjusted to pH = 2 to avoid hydrolysis.

4.2.2 Equipment

A JEOL TEM 2010 (JEOL, Japan) transmission electron microscope was operated at 200 kV. Samples were prepared by sonicating 1 mg precipitates in 1 mL hexane, and a drop of the suspension was put onto a formvar/carbon film supported TEM Cu grid. The Up-conversion fluorescence spectra were measured using a LS-55 luminescence spectrometer (Perkin-Elmer) with an external 980 nm laser diode (1 W, continuous wave with 1 m fiber, Beijing Viasho Technology Co.) as the excitation source in place of the xenon lamp in the spectrometer. The spectrometer was operated at the bioluminescence mode, with gate times of 1 ms, delay time 1 ms, cycle 20 ms, flash count 1 and slip width 10 nm. Photographs were taken by using a Canon Powershot A620 camera (Tokyo, Japan). All samples were measured using the same concentration dispersed in chloroform (~ 0.05 mol/L). XPS analysis was

carried out using a monochromated Al Ka source (1486.5 eV). Elemental scans were based on 20 meV pass energy. Data were collected from the surface without sputtering. The dopants concentration profile from the surface was obtained after sputtering of 1 min, 2 min and 3 min. For each sample, four elements Ca, F, Yb, and Er were measured. The atomic concentrations were calculated through the ratios of integrated peaks area.

4.2.3 Experiment details

The rare earth chlorides were precipitated in excess ammonia, centrifuged and then washed 5 times in de-ionized water. Rare earth trifluoroacetates [$(CF_3COO)_3RE$] were prepared by dissolving respective rare earth hydroxides in trifluoroacetic acid (CF_3COOH), followed by drying in an oven at 80 ^{o}C. Calcium trifluoroacetate [$(CF_3COO)_2Ca$] were prepared by dissolving calcium carbonate ($CaCO_3$) into trifluoroacetic acid.

The previous snthesised 0.1 mmol CaF_2:Yb, Er nanocrystals were used as seeding materials for shell deposition. The precursors 0.1 mmol for undoped CaF_2 shell (CF_3COOCa in OM) were added in and mixed in the 50mL 3-neck flasks using a magntic stirrer, where the CaF_2:Yb,Er nanocrystals served as the seeds on which the undpoed CaF_2 nucleate to form the shell. The reaction procedure for depositing the undoped CaF_2

shell was the same as that used to synthesize CaF_2:Yb,Er nanocrystals. By adjusting the amout of undoped CaF_2 preccossor, the shell thickness could be controlled. Similarly, the CaF_2(core)/CaF_2:Yb,Er(shell) was achieved using CaF_2 NPs as the core with deposition of CaF_2:Yb,Er shell.

4.3 Results and discussion

4.3.1 Morphology

As-synthesized nanocrystals of CaF_2:Yb,Er(core)/CaF_2(shell) were easily dispersed in hexane or chloroform to form a transparent colloidal solution. Using TEM bright field image (**Figure 4.1** B-E), the average particle size of CaF_2:Yb,Er(core)/CaF_2(shell) structure were estimated as ~ 6.9 nm ± 1.2 nm, ~ 8.3 nm ± 1.2 nm, ~ 10.4 nm ± 1.9 nm, ~ 14.1 nm ± 3.4 nm respectively, by counting 100 particles. Compared with the CaF_2:Yb,Er(core) (**Figure 4.1** A and also the same as **Figure 3.4**), the shell thickness were estimated to be ~ 0.8 nm, ~ 1.5 nm, ~ 2.5 nm and ~ 4.4 nm respectively. Note that the size of the CaF_2:Yb,Er(core) was ~ 5.4 nm ± 0.9 nm (**Figure 3.4**, **Figure 4.1**).

The lattice parameter difference between $(Ca_{0.8}Yb_{0.2})F_{2.2}$ (a = b = c = 5.4815 Å, JCPDS file number PDF 87-0976) and CaF_2 (a = b = c = 5.47 Å, JCPDS file number PDF 65-0535) is only ~ 0.2%, making it possible for epitaxial

growth of the undoped shell on the doped core. This was comfirmed by the consistent lattice fringes from the core to the surface of the core-shell structure (**Figure 4.1** B, inset).

For the QDs which used a totally different materials to form the shell such as CdSe(core)/ZnS(shell) structure, there would be a change of at the core/shell interface, indicating the core/shell sturcture [73]. However, for the CaF_2:Yb,Er(core)/CaF_2(shell) sturcture, the undoped CaF_2 shell was the same materials as that of the host, hence the diffraction contrast due to dopants of Yb and Er could not be observed.
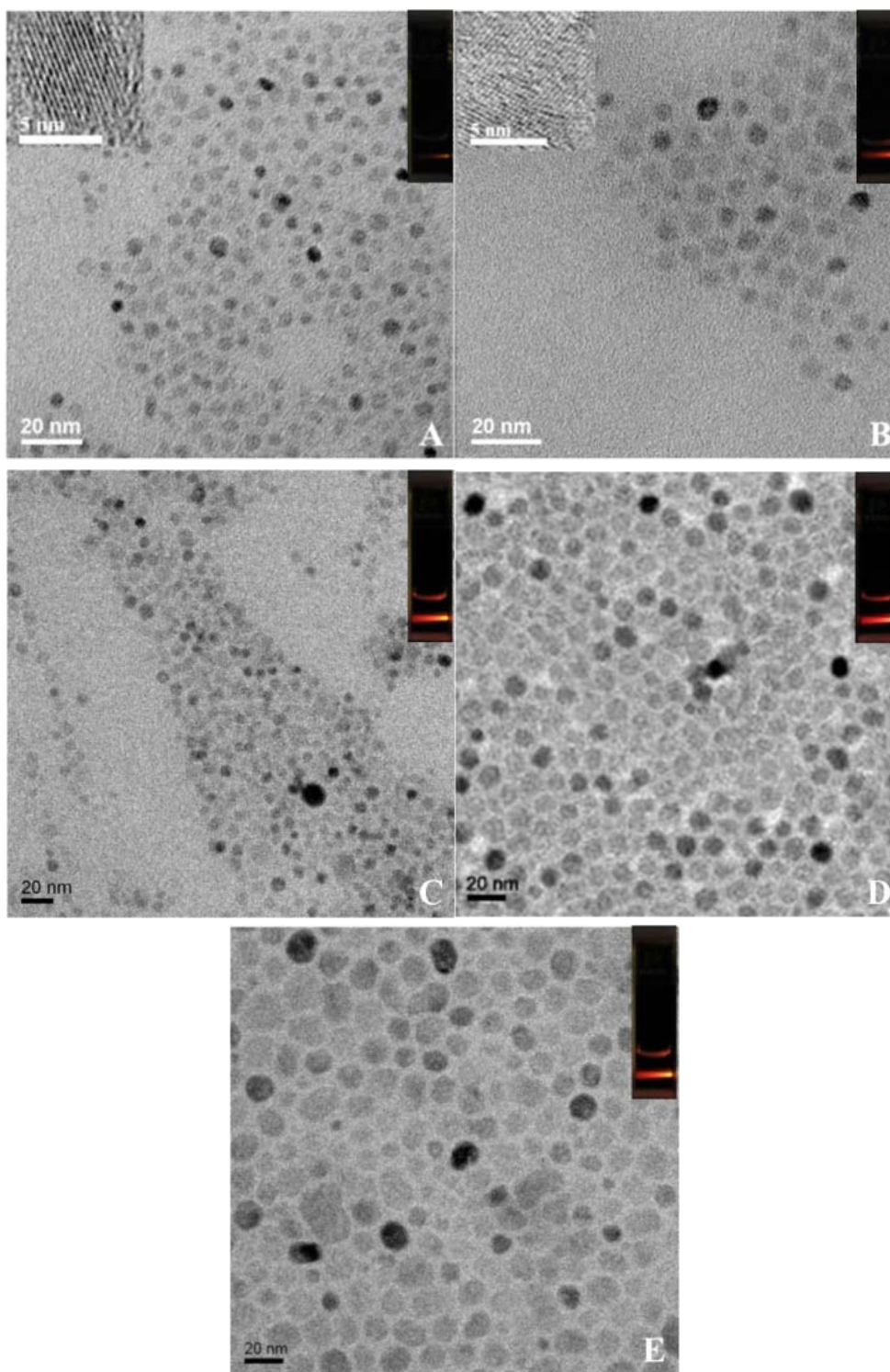
Figure 4.1 Typical TEM bright field image of the A: CaF_2:Yb,Er(core); B-E: CaF_2:Yb,Er(core)/CaF_2(shell) with different shell thickness (B: ~ 0.8 nm, C: ~ 1.5 nm, D: ~ 2.5 nm, E: ~ 4.4 nm). Insets are the up-conversion luminescence taken by camera of corresponding as-synthesized UCNPs.

4.3.2 Room temperature luminescence

Compared with CaF_2:Yb,Er core, the emission intensity increased significantly after coating the core with an undoped CaF_2 shell (inset of **Figure 4.1** A-E). It should be noted that all the samples were under the same concentrations ~ 0.05 M and the camera was set at the same parameters.

All of these RE^{3+} doped nanoparticles showed red luminescence under 980 nm laser excitation. The intensity of CaF_2:Yb,Er(core) (**Figure 4.1** A inset) appeared to be the lowest and it increased dramatically after coating with undoped CaF_2 shell with different thickness (**Figure 4.1** B-E inset).

The room-temperature up-conversion fluorescence spectra of the colloidal CaF_2:Yb,Er(core) and CaF_2:Yb,Er(core)/CaF_2(shell) nanocrystals with different shell thickness under 980 nm NIR excitation is shown in **Figure 4.2**. The peak at 545 nm was assigned to Er transitions from $^4S_{3/2}$ to $^4I_{15/2}$ (green emission) and the peak at 660 nm was assigned to Er transitions from $^4F_{9/2}$ to $^4I_{15/2}$ (red emission). The higher red emission peak contributed to the observed red color. The emission peak position did not show observable shift, indicating the energy level of Er^{3+} remained the same. **Figure 4.3** shows the significant increase of emission intensity of the UCNPs with increasing undoped CaF_2

shell thickness up to ~ 2.5 nm. An increase in shell thickness to 4.4 nm did not

result in total intensity improvement, showing that the critical shell thickness

appeared to be ~ 2.5 nm for these particles.
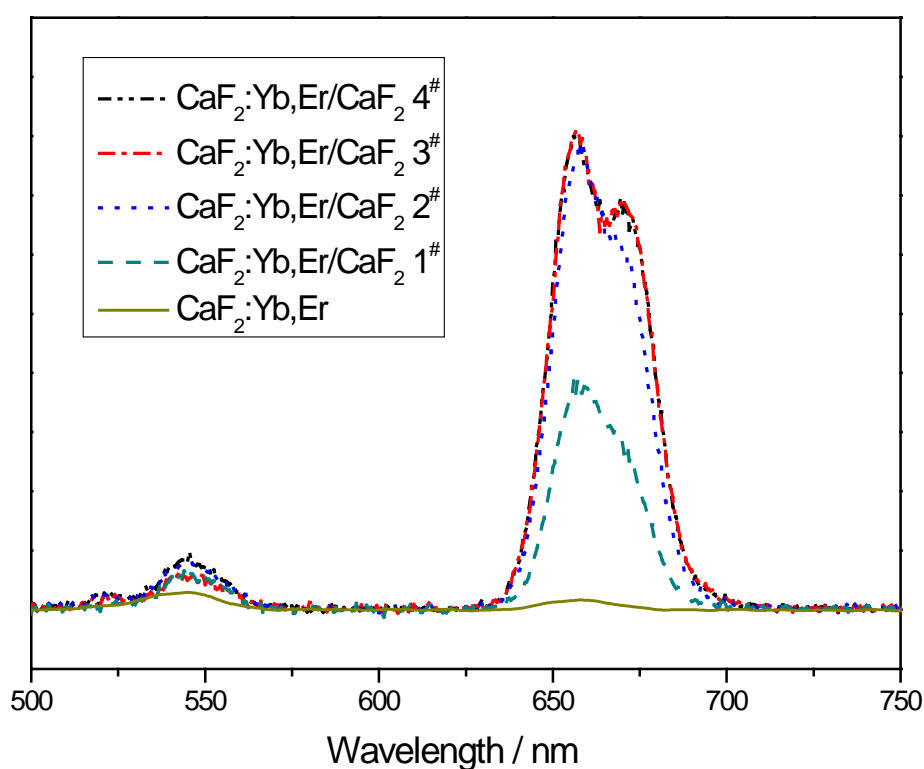
Figure 4.2 Up-conversion fluorescence spectra of CaF_2:Yb,Er (core) and CaF_2:Yb,Er(core)/CaF_2(shell) with different shell thickness 1[#] (~ 0.8 nm), 2[#] (~ 1.5 nm), 3[#] (~ 2.5 nm), 4[#] (~ 4.4 nm)
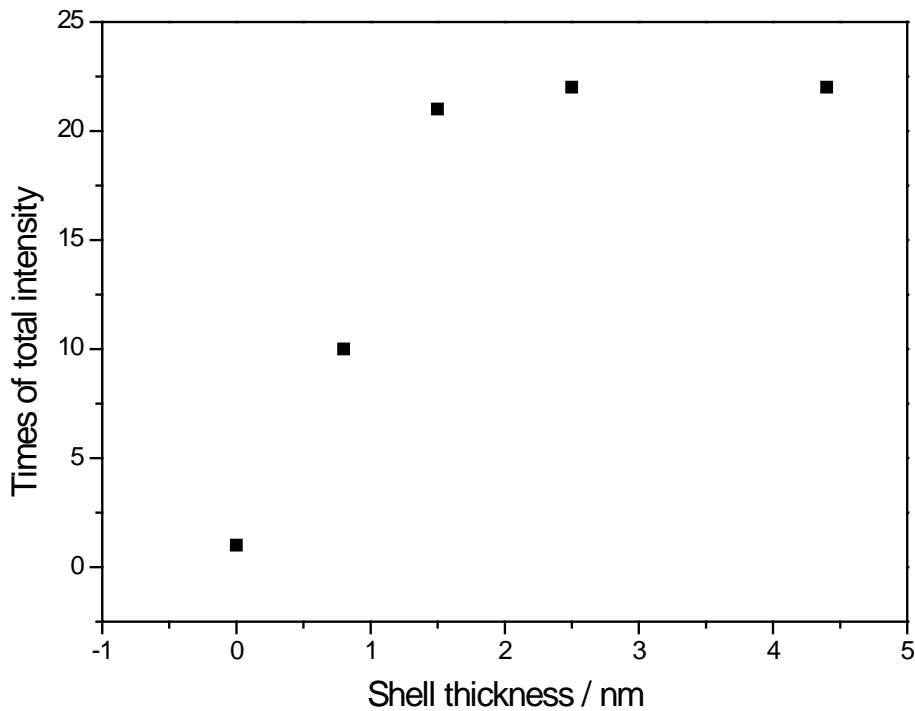
Figure 4.3 The relationship of total emission intensity enhancement of CaF_2:Yb,Er/CaF_2 nanoparticles of different shell thickness of undoped CaF_2.

4.3.3 Up-conversion process

Using Dieke energy-level diagram [5], the UC processes of CaF_2:Yb,Er was discussed (**Figure 4.4**). The 4f-4f electric dipole transition is Laporte forbidden for an Er^{3+} ion, resulting in low transition probabilities. The life time of Er^{3+} at excited states was determined to be about hundreds of μs [2], which is essential for UC luminescence.

First, Yb^{3+} ions were excited by the 980-nm NIR photons from the ground state $^2F_{7/2}$ to the excited state $^2F_{5/2}$ (this energy gap is nearly the same to the energy of 980-nm photon). It transferred its energy to the activator Er^{3+} to excite it

from ground state $^4I_{15/2}$ to the excited state $^4I_{11/2}$. Er^{3+} was then further pumped to $^4F_{7/2}$ excited state by another energy transfer from $^2F_{5/2}$ of Yb^{3+} ion.

Green light

Followed by a multi-phonon relaxation process, Er^{3+} lost part of its energy from excited state $^4F_{7/2}$ to lower excited state $^4S_{3/2}$, then returned to ground state $^4I_{15/2}$, emitting green light.

Red light

For red emission, there are two possible routes:

(i)   Cross-relaxation process $|^4I_{15/2}, ^4S_{3/2}> \rightarrow |^4I_{13/2}, ^4I_{9/2} >$ of Er^{3+} [85]

When Er^{3+} was excited to the $4S^{3/2}$ state, it did not recombine to the ground state to emit green light. Instead, it would undergo a non-radiative energy transfer process to return to a lower energy level $^4I_{9/2}$, while exciting another Er^{3+} ions to reach its $^4I_{13/2}$ excited state. Followed by another energy tranfer from Yb^{3+} to Er^{3+}, it consequently increased the population in the $^4F_{9/2}$ state, eventually leading to red emission. This fast non-radiative cross-relaxation process was closely related to the distance between Er ions.

(ii)   Multi-phonon relaxation from $^4I_{11/2}$ to $^4I_{13/2}$ of Er^{3+}

This process occurred after Yb^{3+} transferred its energy to Er^{3+} to reach $^4I_{11/2}$ state. Assisted by the phonon relaxation, Er^{3+} may lose its energy to $^4I_{13/2}$

before absorbing another 980-nm NIR photon to further excite Er^{3+} to $^4F_{9/2}$ state, followed by red emission when went back to ground state.

The red light dominated phenomenon could be explained by the fast non-radiative cross-relaxation process, which might result from segregation of Er^{3+} on the core, [84] cluster formation of RE^{3+} ions in CaF_2 host [86] and other defects. Consequently, it increased the population in $^4F_{9/2}$ state, which was responsible for the red luminescence colour.
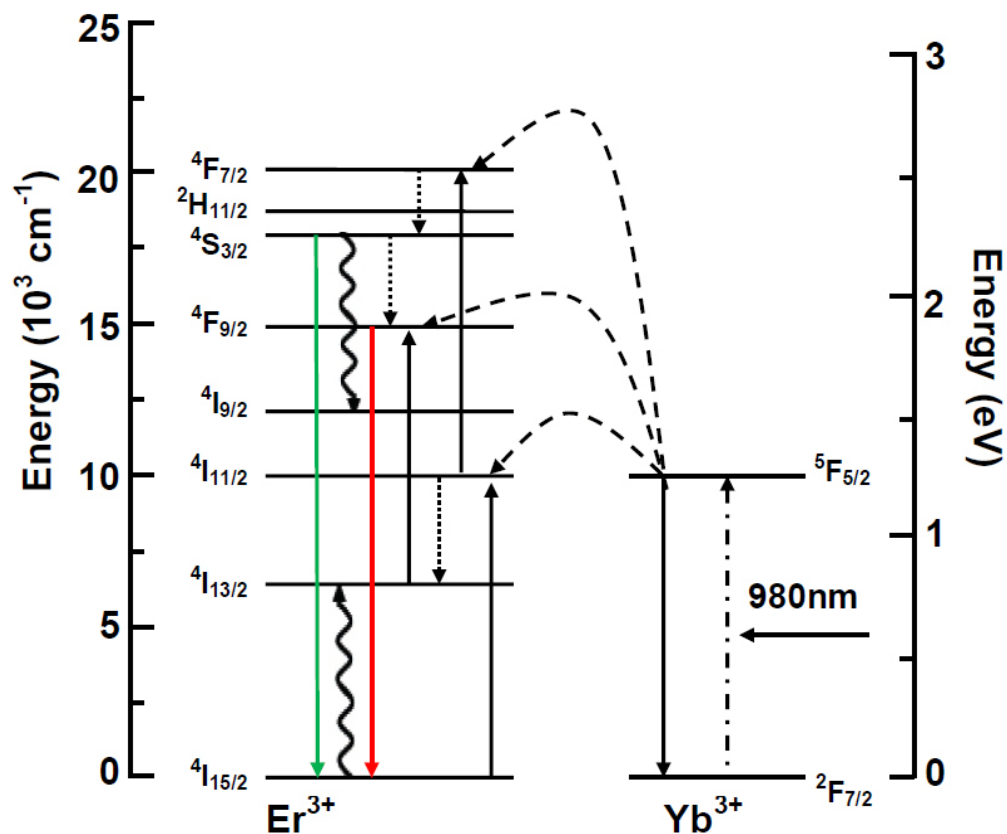
Figure 4.4 The UC processes CaF_2:Yb,Er nanocrystals under 980-nm diode laser excitation. The dashed-dotted, dashed, dotted, and full arrows represent photon excitation, energy transfer, multi-phonon relaxation, and emission processes, respectively. The pair of arrows with curve shows the cross-relaxation process. Only visible and NIR emissions are shown here

4.3.4   Core/shell structure and intensity enhancement

As CaF_2:Yb,Er(core)/CaF_2(shell) structure could not be determined by the TEM contrast different, XPS measurements were conducted.

Figure 4.5 shows the surface atomic concentration of Yb and Er as a function of the undoped shell thickness, while the core was the same. The correlation that the atomic concentration of Yb and Er decreases as the shell thickness increases can be found. XPS, used for surface analysis, its penertration depth (information depth) is ~ 1 nm for the Al Kα photon source (1486.5 eV) (**Figure 4.6**). This explains why the 0.8 nm sample showed relatively high RE concentration, as the undoped shell thickness was silimilar to that of information depth.
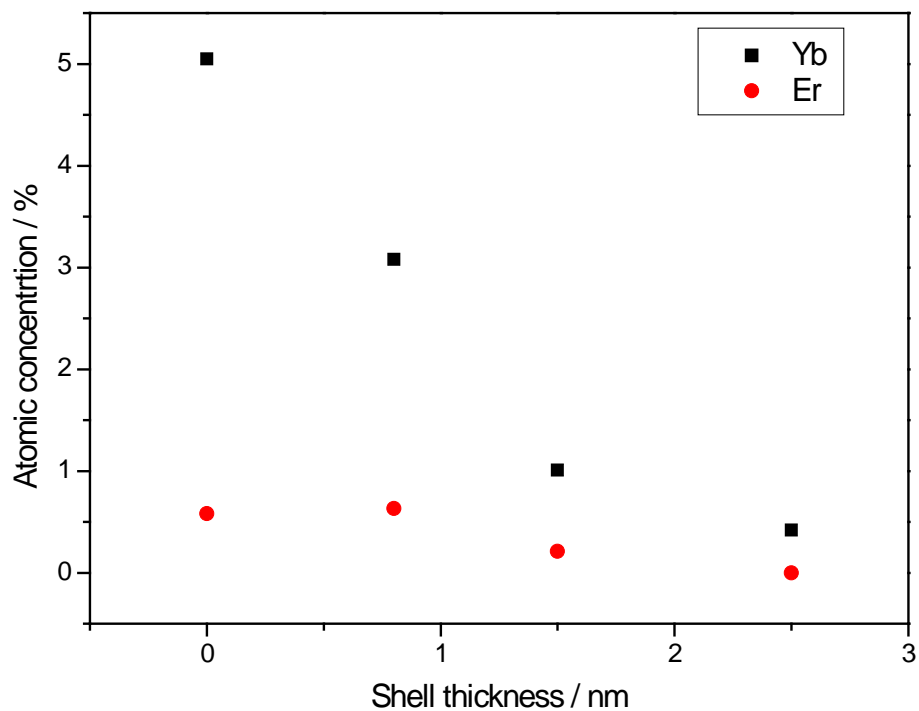
Figure 4.5 The atomic concentration of Yb and Er on the surface of the CaF$_2$:Yb,Er(core)/CaF$_2$(shell) structure with different shell thickness, obtained by XPS without sputtering.
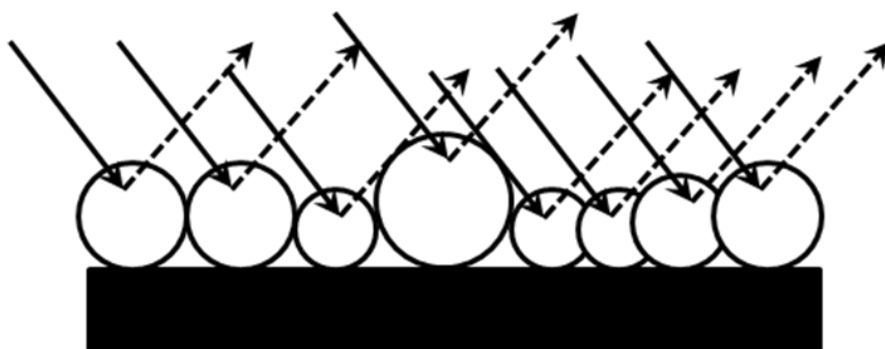
Figure 4.6 A schematic of the information depth of the XPS

Figure 4.7 shows the average Yb and Er atomic concentration of several particles after sputterring at different periods of time (0 min, 1 min, 2 min and 3 min) for CaF_2:Yb,Er(core)/CaF_2(shell) with shell thickness of 2.5 nm. It can be found that the Yb and Er concentration increased with sputtering time.

From doped CaF_2:Yb,Er core to CaF_2:Yb,Er(core)/CaF_2(shell) with thicker shell, the decrease of Yb and Er on the surface was observed, confirmning the growth of the undoped CaF_2 on CaF_2:Yb,Er(core) to form the core/shell structure.
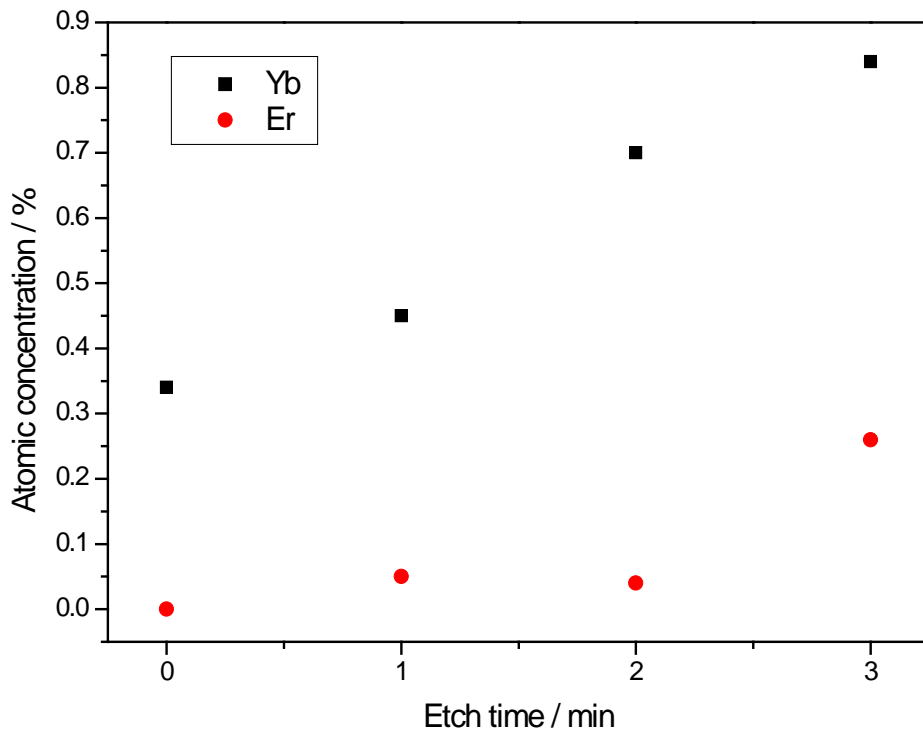
Figure 4.7 Concentration of Yb and Er after sputtering for different times (0 min, 1 min, 2 min and 3 min) on CaF_2:Yb,Er(core)/CaF_2(shell), with original undoped shell thickness to be ~ 2.5 nm.

The RE ion diffusion in CaF_2 in bulk materials was reported, which was rather slow (it takes times in the order of the age of earth to diffuse to a scale of 100 μm at ~ 500 ^{o}C, 1 atm [87]). Using the diffusion constant and activiation energy reported in bulk materials [87], Yb ion diffusion was estimated to obtain a general idea of the RE ions diffusion from doped CaF_2:Yb,Er(core) to undoped CaF_2(shell). This estimation was based on a semi-infinite model, i.e. concentration-independent diffusion, simple one-dimensional with a constant concentration of source reservoir. The point 0.1 nm from the doped core was selected to calculate the concentration. **Table 4.1** shows the calculated Yb concentration on the undoped shell at different temperature. The RE diffusion in CaF_2 appeared to be negligeable (**Table 4.1**) at 613.15K for 1 h based on the above estimation. **Figure 4.8** shows the use of effective disffusion length $(4Dt)^{1/2}$ to estimate the diffusion distance at different temperatures. It showed that Yb diffusion would only be significant above ~ 800 K. However, it should be noted that surface energy of nano materials may be much larger than that of bulk one [88], therefore the ion diffusion could not be completely ruled out.

Table 4.1 Calculated Yb diffusion on undoped shell at different temperature.

$t/°C$	T/K	$D_{yb} / m^2 s^{-1}$	$2*(Dt)^{1/2} / m$	$erf\ [x/(2*(Dt)^{1/2})]$	$c(x)/\%$
25	298.15	1.95×10^{-70}	1.68×10^{-33}	1	0
60	333.15	3.64×10^{-63}	7.24×10^{-30}	1	0
100	373.15	1.58×10^{-56}	1.51×10^{-26}	1	0
140	413.15	3.57×10^{-51}	7.17×10^{-24}	1	0
180	453.15	9.14×10^{-47}	1.15×10^{-21}	1	0
220	493.15	4.51×10^{-43}	8.06×10^{-20}	1	0
260	533.15	6.20×10^{-40}	2.99×10^{-18}	1	0
300	573.15	3.12×10^{-37}	6.70×10^{-17}	1	0
340	613.15	6.95×10^{-35}	1.00×10^{-15}	1	0
380	653.15	7.99×10^{-33}	1.07×10^{-14}	1	0
420	693.15	5.32×10^{-31}	8.75×10^{-14}	1	0
460	733.15	2.24×10^{-29}	5.67×10^{-13}	1	0
500	773.15	6.39×10^{-28}	3.03×10^{-12}	1	0
540	813.15	1.31×10^{-26}	1.37×10^{-11}	1	0
580	853.15	2.03×10^{-25}	5.41×10^{-11}	0.99106958	0. 0893
620	893.15	2.46×10^{-24}	1.88×10^{-10}	0.547606833	4.5239
660	933.15	2.40×10^{-23}	5.88×10^{-10}	0.189914357	8.1009
700	973.15	1.95×10^{-22}	1.68×10^{-9}	0.067266763	9.3273

Remarks： Semi-infinite diffusion model was used to calculate the

where diffusion constant $(D_{Yb})=3.1\times10^{-1} \exp(-395\ kJ\ mol^{-1}/RT)$ m^2/s[87]; R is gas constant; duration of the annealing time (t)= 3600s; concentration of diffusant (c) = 20%; depth chosen to calculate on the undoped CaF_2 from core (x)=0.1 nm; erf refers to the complementary error function.
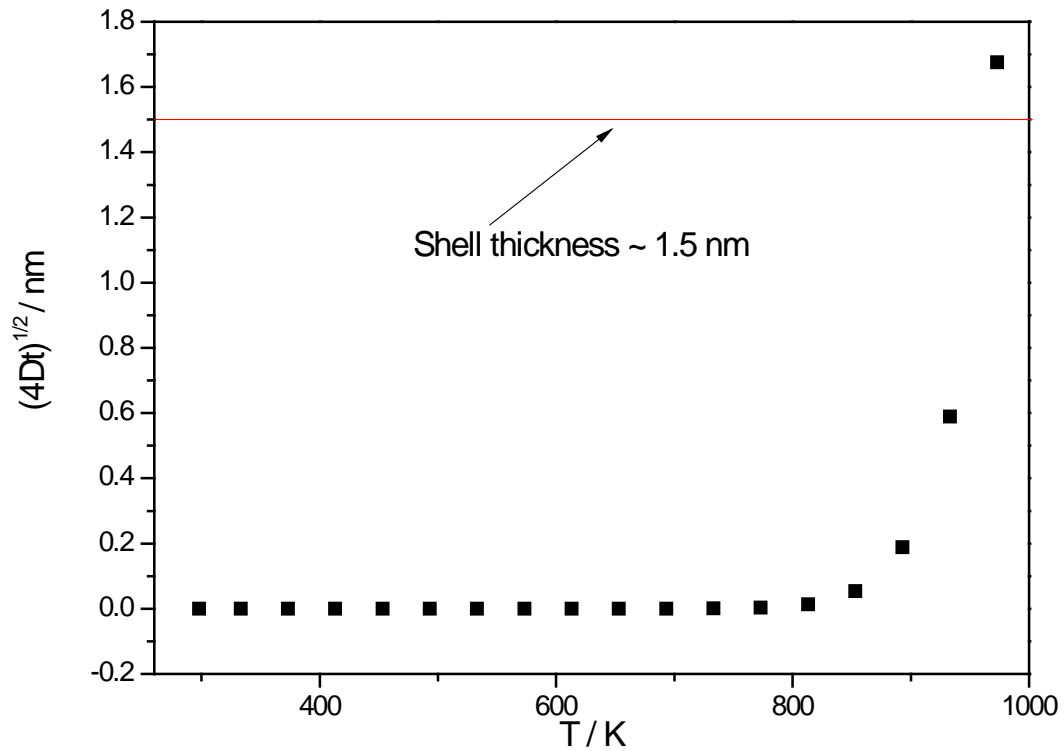
Figure 4.8 Estimated effective diffusion length of Yb in CaF$_2$ at different temperature

The importance of undoped shell materials is that the local environment of the doped ions on the surface may be significantly different from that of the interior doped ions [3, 4]. For nano particles, this effect can be more significant as the surface-to-volume ratio is much higher than that of bulk. Without an undoped shell, the ions residing on the surface would be subject to the following:

i.   Lack of crystal field strength

As the ions stay on the surface are not surrounded by the host materials, the

crystal field of the surface ions is much weaker than that of the ones inside. Although the 4f electrons of RE^{3+} were shielded by the completely filled $5s^2$ and $5p^6$ shells, the crystal field would influence the energy transition process thus affecting the total efficiency.

ii. Exposure to high vibration modes

As mentioned in the introduction, luminescence may be quenched by the high energy phonons. Undergoing a multi-phonon relaxation process, the excited ions may lose its energy as heat instead of luminescence. This process was not significant for the ions protected by the low phonon energy host materials. However, the surface ions may be readily quenched by high energy phonon vibration modes which came from surface impurities, ligands, defects and solvents (above 1000 cm^{-1})

iii. Energy transfer from interior to surface trough dopants

The excitation energy of interior ions could transfer its energy to the surface ions through adjacent doping ions. The interior RE ions may eventually be quenched by the energy transfer as well.

Due to the above, an insert crystalline shell provided a strong crystal field for surface ions, protecting them from the high vibration groups on the surface which caused non-radiative relaxation processes. Eventually, the total

intensity was increased. The critical shell thickness appeared to be ~ 2.5 nm. The 0.8 nm shell did not seem to provide a sufficient protection, whereas 4.4 nm shells did not result in further emission increase. It has been found that the electric dipole-dipole resonance energy transfer process will occur when the distance is in order of ~ 1 nm [4]. The 0.8 nm shell might not be thick enough to prevent the non-radiative relaxation due to interactions with the environment. When the thickness reached ~ 2.5 nm, the shell would possibly provide a complementary crystal field to the RE^{3+} ions found on the surface of the doped core and present a sufficient barrier to non-radiative multi-phonon relaxation induced by the environment.

4.3.5 Surface/ Volume ratio

As discussed above, the surface condition has a great influence on the total intensity of UCNPs. To further understand this effect, the following studies were pursued.

The CaF_2(core)/CaF_2:Yb,Er(shell) structures with different shell thickness of doped shell were made (**Figure 4.9**). The doped CaF_2:Yb,Er were used as the shell to better "feel" the environment. The average particle size of CaF_2(core)/CaF_2:Yb,Er(shell) structure were estimated to be ~ 6.1 nm ± 1.1 nm, ~ 7.8 nm ± 1.5 nm, ~ 9.4 nm ± 1.8 nm, respectively, from the TEM

bright field images. The corresponding photoluminescence spectra is shown

in **Figure 4.10**, which was normalized to the same amount of doped
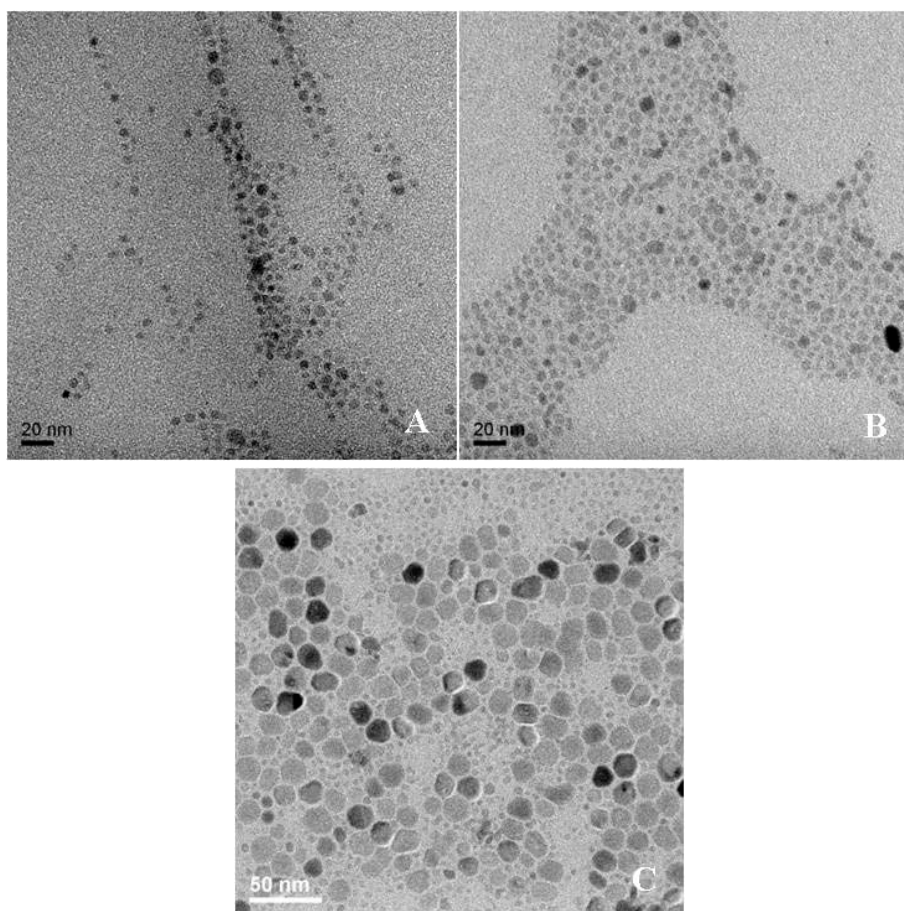
CaF_2:Yb,Er.

Figure 4.9 TEM bright field image of CaF_2 (core)/CaF_2:Yb,Er (shell) 1[#]-3[#] with different shell thickness (1[#]: ~ 0.4 nm, 2[#]: ~ 1.2 nm, 3[#]: ~ 2nm).
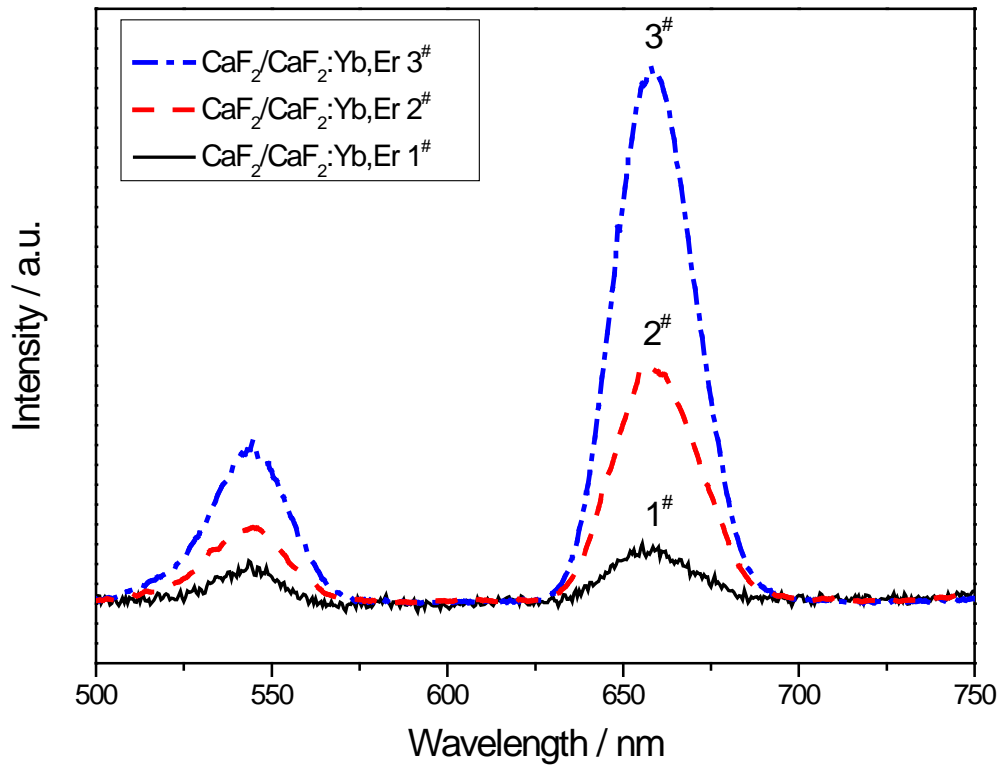
Figure 4.10 Up-conversion fluorescence spectra of CaF_2(core)/CaF_2:Yb,Er (shell) $1^\#$-$3^\#$ with different shell thickness ($1^\#$: ~ 0.4 nm, $2^\#$: ~ 1.2 nm, $3^\#$: ~ 2 nm) after normalizing to the same amount of doped CaF_2:Yb,Er

From CaF_2(core)/CaF_2:Yb,Er(shell) $1^\#$ to $3^\#$, the surface area increased with d_n^2 while the volume of CaF_2:Yb,Er increased with d_n^3, resulting in the decrease of surface-to-volume ratio from 1.43 to 0.39. At the same time, the intensity of CaF_2(core)/CaF_2:Yb,Er(shell) $1^\#$ to $3^\#$ increased from 33 to 248. This result shows the inverse relation between surface-to-volume ratio and the total intensity (summarized in **Table 4.2**).

Table 4.2 The comparison of CaF_2(core)/CaF_2:Yb,Er(shell) structure with different shell thickness

Sample	1#	2#	3#
Total size (d_n) / nm	~ 6.1 nm ± 1.1 nm	~ 7.8 nm ± 1.5 nm	~ 9.4 nm ± 4.8 nm
Shell thickness (d_s) / nm	~ 0.4 nm	~ 1.2 nm	~ 2 nm
Surface area (A_n) / nm²	468	765	1110
Volume of CaF_2:Yb,Er (V_n) / nm³	327	1364	2855
Surface-to-volume ratio	1.43	0.56	0.39
Intensity / arbitrary unit	33	120	248

Remarks: 1. $A_n = \pi \left(\frac{d_n}{2}\right)^2$; ; surface-to-volume

ratio: $\frac{A_n}{V_n}$

where A_n refers to surface area; d_n refers to total particle size; d_0 is the undoped CaF_2 core size (~ 5.4 nm ± 0.9 nm).

2. The white ball refers to the undoped core CaF_2, while brown area refers to the doped shell CaF_2:Yb,Er.

Furthermore, the up-conversion fluorescence spectra of CaF_2:Yb,Er(core)/CaF_2(shell) and CaF_2(core)/CaF_2:Yb,Er(shell) with similar particles size (~ 6.9 nm ± 1.2 nm and ~ 6.1 nm ± 1.1 nm respectively) was compared (**Figure 4.11**).

The up-conversion fluorescence spectra were normalized to the amount of CaF_2:Yb,Er. The intensity of CaF_2:Yb,Er(core)/CaF_2(shell) was much higher (~ 6 times) than that of CaF_2(core)/CaF_2:Yb,Er(shell) (summarized in **Table 4.3**). It should be noted the main difference of these two kind of samples is the location of the RE dopants, while their sizes were quite similar. The first sample had the RE dopans protected by the undoped shell , while the second one exposed the RE dopants to the surface. In spite of the fact that the external field does not tend to affect the RE ions on their intrinsic optical properties such as sharp emssion lines, it does affect the electron and phonon interactions.
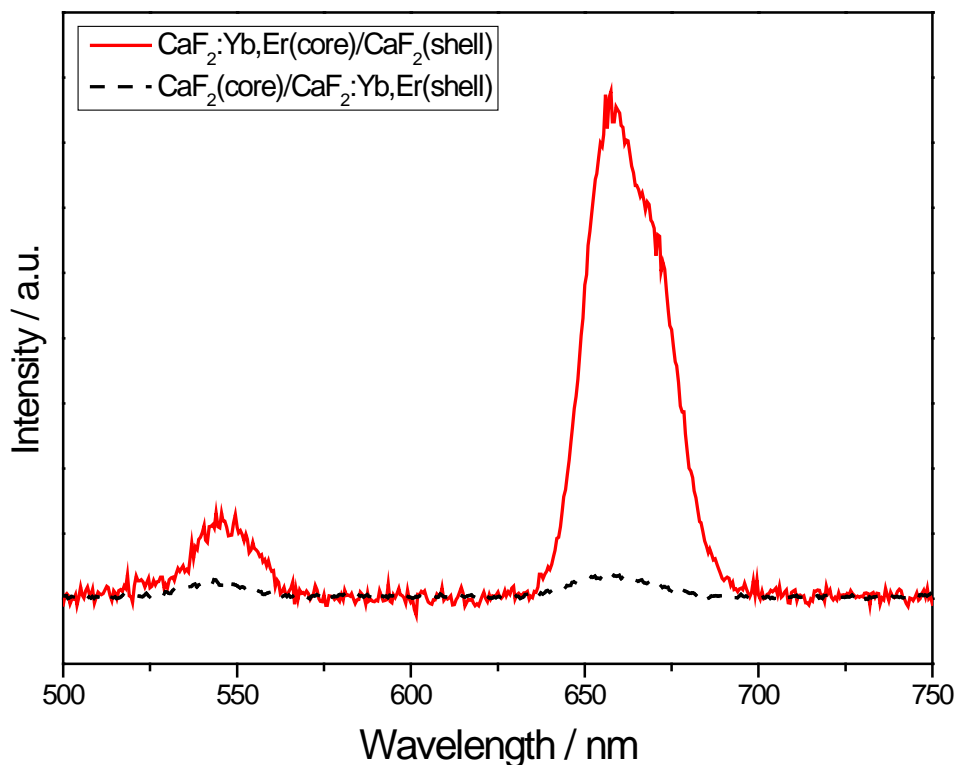
Figure 4.11 Up-conversion spectra of CaF_2:Yb,Er(core)/CaF_2(shell) (~ 6.9 nm ± 1.2 nm) and CaF_2(core)/CaF_2:Yb,Er(shell) (~ 6.1 nm ± 1.1 nm)

Table 4.3 The comparison of CaF_2:Yb,Er(core)/CaF_2(shell) CaF_2(core)/CaF_2: Yb,Er (shell) with similar particle size

Sample	CaF_2:Yb,Er(core)/CaF_2(shell)	CaF_2(core)/CaF_2:Yb,Er (shell)
Total size / nm	~ 6.9 nm ± 1.2 nm	~ 6.1 nm ± 1.1 nm
Intensity / a.u.	110	18

These results confirmed that the surface condition greatly influenced the total intensity, indicating the importance of protection from the undoped shell. Although other factors that influence the total emission intensity could not be ruled out, the surface-to-volume ratio of doped CaF_2:Yb,Er was demenstrated as a key parameter on the emission intensity.

4.4 Summary

Using CaF_2:Yb,Er nanocrystal as seed, the epitaxial growth of CaF_2 was achieved to form the CaF_2:Yb,Er(core)/CaF_2(shell) structure, with different shell thickness ~ 0.8 nm, ~ 1.5 nm, ~ 2.5 nm and ~ 4.4 nm (corresponding total particles size ~ 6.9 nm ± 1.2 nm，~ 8.3 nm ± 1.3 nm，~ 10.4 nm ± 1.9 nm and ~ 14.1 nm ± 3.4 nm, respectively). The room temperature luminescence spectra indicated the undoped shell greatly increased the total intensity. The critical shell thickness was estimated to be ~ 2.5 nm with enhancement more than 20 times.

A series of different size of CaF_2(core)/CaF_2:Yb,Er(shell) structure, with particles size ~ 6.1 nm ± 1.1 nm, ~ 7.8 nm ± 1.5 nm, ~ 9.4 nm ± 1.8 nm, respectively, was also produced to investigate the factors that affect the total intensity. The result shows that the total intensity was greatly influenced by the environment of RE dopants. When there was no undoped protective shell, the total intensity decreased as the ratio of surface-to-volume increased.

Chapter 5

5 Silica Coating on CaF$_2$Yb,Er(core)/CaF$_2$(shell)

5.1 Introduction

Using these UCNPs nanocrystals directly for biological applications is impossible, because most of as-synthesized UCNPs are hydrophobic while the biological system is aqueous in nature. The conjugation site is also required to enable attachment of functional molecules for various biomedical applications. As a result, surface functionalization of the as-synthesized UCNPs is needed.

Recently, quite a few methods for surface functionalization were reported and reviewed [3], such as ligand exchange, ligand oxidization, ligand attraction, layer by layer assembly, and amorphous silica coating. As amorphous silica is chemically and thermally inert in body fluid environment, silica coating may improve the photo-stability and chemical-stability [51]. The –OH group on silica surface will greatly increase the water-solubility of the coated NPs, providing a good linking site at the same time. The silica coating also provides an additional flexibility of particle design. As demonstrated by Zhang and

co-workers, embedding QDs and dyes inside silica shells led to multicolour emission [52]. Silica coating is therefore one of the most convenient methods for surface functionalization.

In this chapter, silica coating on the $CaF_2Yb,Er(core)/CaF_2(shell)$ was produced. The silica coating not only made the UCNPs become water-redispersable but also provided a linking site, demonstrating the potential of CaF_2:Yb,Er UCNPs for bio-application

5.2 Method

5.2.1　Chemicals

Tetraethylorthosilicate (TEOS) ($Si(OC_2H_5)_4$, 98%) was obtained from APS Finechem,. Polyoxyethylene (5) nonylphenylether (NP-5) (or Igepal CO-520), 1-Hexanol ($CH_3(CH_2)_5OH$), acetone (($CH_3)_2CO$) and ethanol (CH_3CH_2OH, analytical reagent grade) were purchased from Sigma-Aldrich without further purification. The CaF_2:Yb,Er(core)/CaF_2(shell) UCNPs were synthesized as chapter 3 described.

5.2.2　Equipment

Zeta potential measurement was performed by using a Malvern Zetasizer

Nano ZEN3600 (UK). Fourier transform infrared (FTIR) spectra were measured using a Varian FT3100 spectrometer (Palo Alto, CA). 1 mg of precipitates was re-dispersed in hexane and then deposited on a KBr pellet.

5.2.3 Experiment details

The most commonly used approaches to deposit silica on nanocrystals are the sol-gel derived "Stöber method" [89] and the micro-emulsion methods [90]. The Stöber method can only be used for hydrophilic nanocrystals which are able to disperse well in polar solvents such as ethanol and water. The total particle size and size distribution of the silica-coated nanoparticles obtained by these methods however are not well controlled. Microemulsion methods, however, are able to coat silica on the hydrophobic nanocrystals. It has been used for CdSe QDs [91], Fe_3O_4 nanoparticles [92] and $NaYF_4$:Yb,Er {Qian, 2009 #454} which was also adapted for this work.

Surfactants of Igepal CO-520 (1.8 mL) and 1-hexanol (1.0 mL) were dispersed in cyclohexane (7 mL) by mechanical stirring. A solution of CaF_2:Yb,Er(core)/CaF_2(shell) nanoparticles in cyclohexane (200 mL, 0.2 mg/mL) was added. The resulting mixture was stirred, and ammonium hydroxide (NH_3·H_2O 50 mL, 28%) was added to form a transparent reverse microemulsion. This solution was stirred for 2 h before TEOS (3 mL) was

added. The reaction was continued for 24 h. The CaF$_2$:Yb,Er/CaF$_2$/silica nanoparticles were collected by centrifuging and washing, then re-dispersed in acetone, ethanol, or deionized water. In the Zeta potential test, the CaF$_2$:Yb,Er/CaF$_2$/silica was dispersed in the de-ionized water and 1M HCl and 1M NaOH were used as the acid and base solution. The pH meter were calibrated using buffer solution of pH=4 and pH=10 respectively. A mechanical pump was used for adding the acid and base to adjust the pH.

5.3 Results and discussion

Figure 5.1 shows the TEM bright field images of CaF$_2$:Yb,Er/CaF$_2$/silica dispersed in ethanol. The average size was ~ 30.2 nm ± 1.7 nm. As the CaF$_2$: Yb,Er(core)/CaF$_2$(shell) used here was ~ 7 nm, the silica shell thickness was estimated to be ~ 12 nm (see **Figure 5.1**).
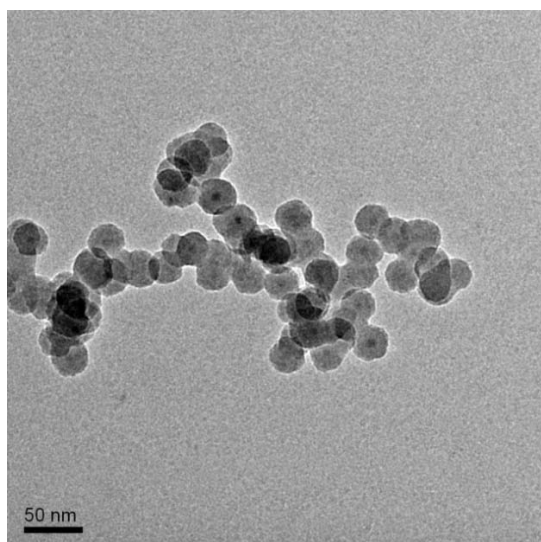

Figure 5.1 TEM bright field image of CaF$_2$:Yb,Er/CaF$_2$/Silica nanoparticles

The existence of silica was then confirmed by the FTIR spectra in **Figure 5.2**. The absorption peaks at 3422 cm^{-1}, 1090 cm^{-1} and 796 cm^{-1} could be attributed to the -OH stretching vibration, Si-O group stretching and bending vibration respectively, indicating the existence of silica. The signature peaks of C=C, CH_2 and NH_2 for OM centered at around 1615/3006 cm^{-1} 2852/2922 cm^{-1} and 1577/3321 cm^{-1} nearly disappeared after the silica coating (summarized in **Table 5.1**), This shows that most of the surfactants have been removed during the micro-emulsion reaction. Note that, on the surface of amorphous silica, Si-O bond network could not be kept in the ratio where each Si atom is linked to 4 O atoms and each O atom to 2 Si atoms. The Si-O- bond would dangle until being terminated by H atom to form Si-OH, providing a –OH group on its surface. This is becomes good linking site for attaching functional molecules used in various biomedical applications.
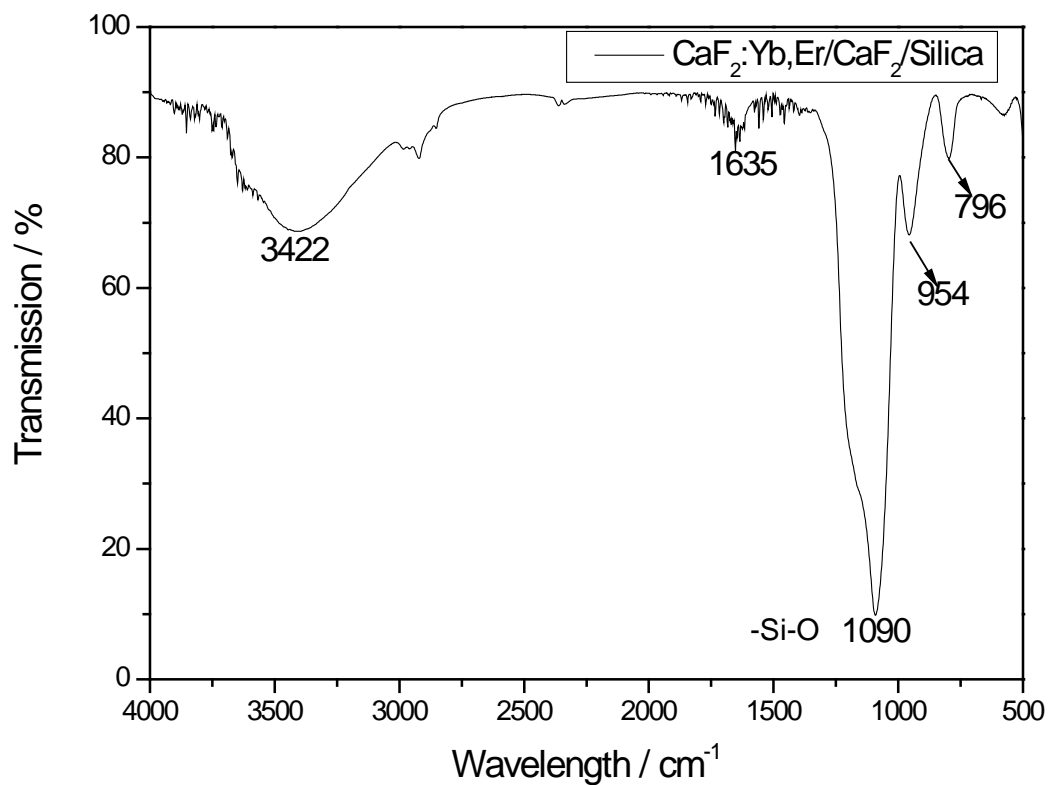
Figure 5.2 FTIR spectra curve of as prepared CaF_2:Yb,Er/CaF_2/Silica nanoparticles

Table 5.1 FTIR peaks assignment for CaF_2:Yb,Er/ CaF_2/Silica nanoparticles

Wavenumber (cm^{-1})	Assignment
3422	O-H stretching vibration
1090	Si-O stretching vibration
796	Si-O bending vibration
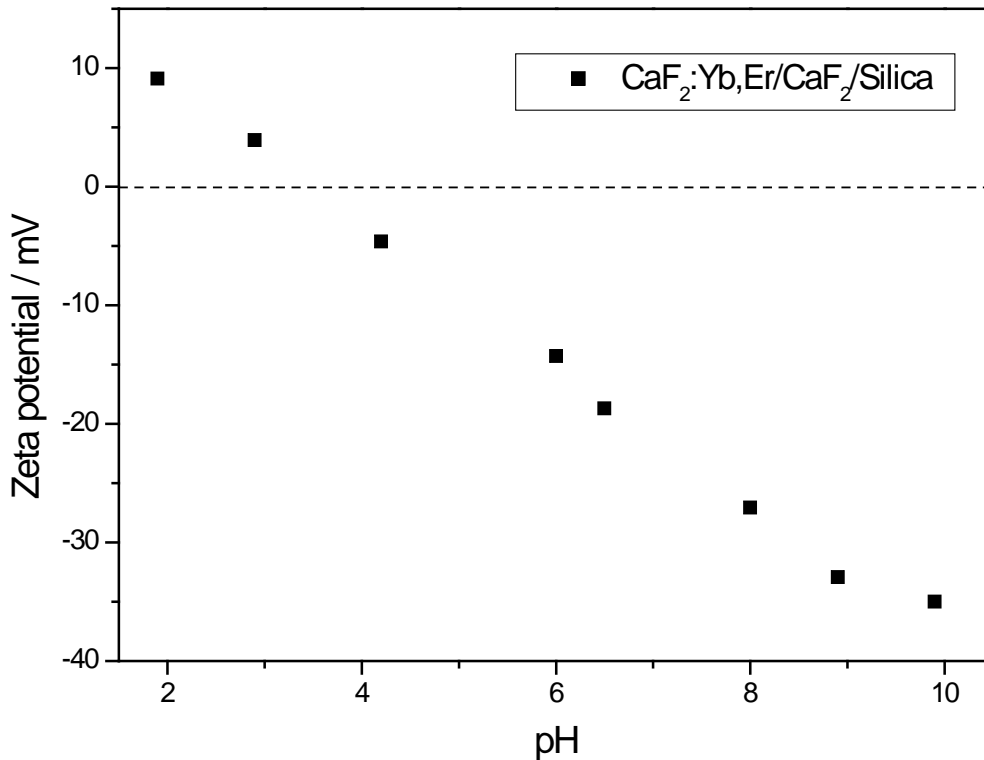
Figure 5.3 Zeta potential of CaF_2:Yb,Er/CaF_2/ Silica nanoparticles dispersed in D.I. water as a function of pH at room temperature

Zeta potential measurements were conducted for CaF_2:Yb,Er/ CaF_2/Silica nanoparticles. As shown in **Figure 5.3**, the isoelectric point (IEP) of the CaF_2:Yb,Er/CaF_2/silica was approximately at pH = 3.5 in D.I. water at room temperature. When pH < 3.5, the surface charge of NPs was positive, indicating the exposed Si-OH group to had adsorbed extra H^+ to form a Si-OH_2^+ group. At pH > 5, the surface became negatively charged, showing that the exposed Si-OH group transformed to Si-O^- group (**Figure 5.4**). Combined with the FTIR results, it confirmed the successful deposition of silica coating. The absolute value of zeta potential was about 30 mV at pH =7, indicating that these silica coated NPs remain stable at this pH with negative

surface charge.
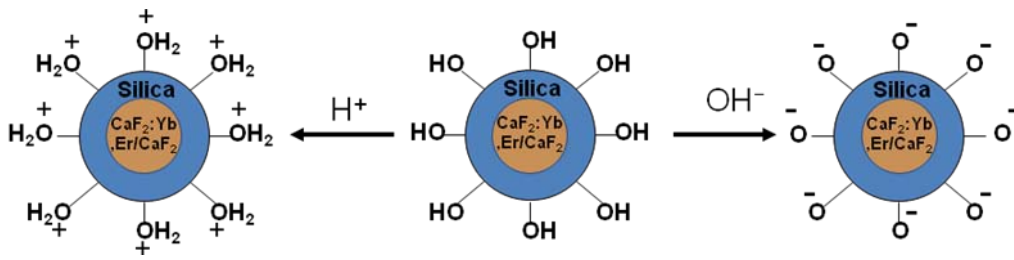
Figure 5.4 Schematic diagram of change of surface properties for CaF_2:Yb,Er/CaF_2/Silica nanoparticles below, at and above the IEP point

The emission intensities before and after the silica coating were not investigated.

In order to record the emission spectrum of monodispersed CaF_2:Yb,Er/CaF_2/silica NPs, they will need to be diluted into much lower concentration. This would lead to poor signal-to-noise ratio under our 1 W NIR laser excitation source, making the measurement to compare relative intensity difficult.

5.4 Summary

Amorphous silica shell was deposited using a micro-emulsion method on CaF_2:Yb,Er/CaF_2 nanoparticles to form CaF_2:Yb,Er/CaF_2/silica sandwich structure with average particles size ~ 30.2 nm ± 1.7 nm.

The silica shell thickness was estimated to be ~ 12 nm. The existence of silica was confirmed by the FTIR and Zeta-potential results. The IEP for this CaF_2:Yb,Er/CaF_2/silica in D.I. water was determined to be pH=3.5. The value of Zeta potential was about -30 mV at pH =7, suggesting that it may be rather stable in bio-environment (pH ~ 7.35). The –OH functional group on surface also provided a good linking site.

Chapter 6

6 Conclusion

Using thermal-decomposition method, CaF_2:Yb,Er up-conversion nanoparticles were successfully synthesized in oleylamine at 340 ^{o}C. The as-synthesized nanoparticles were quite uniform (particle size ~ 5.4 nm ± 0.9 nm) and well dispersed in hexane or chloroform. The UCNPs emitted reddish light under NIR 980 nm excitation.

The undoped CaF_2 was then successfully deposited on the CaF_2:Yb, Er(core) to form the "core-shell" structure with different shell thickness ~ 0.8 nm, ~ 1.5 nm, ~ 2.5 nm and ~ 4.4 nm, respectively. With a ~ 2.5 nm shell, the total intensity was improved by more than 20 times. The improvement of the emission intensity was mainly attributed to the surface effects. The low surface-to-volume ratio had less surface defects per volume, minimizing the non-radiative loss. The nanoparticles with a protecting shell had a much higher emission intensity compared with the one without it. Finally, silica coating was deposited on CaF_2:Yb,Er(core)/CaF_2(shell) UCNPs to render these particles water-dispersible for potential bio-application.

CaF_2:Yb,Er(core)/CaF_2(shell) up-conversion nanoparticles showing strong red emission, with its longer wavelength and penetration depth compared with that

of shorter wavelengths of green and blue lights, may find promising potential

applications.

References

[1] N. Bloembergen, Physical Review Letters 2 (1959) 84.

[2] F. Auzel, Chemical Reviews 104 (2004) 139.

[3] F. W. a. X. Liu*, Chemical Society Reviews 38 (2009) 976.

[4] G.Blasse and B.B.Grabmaier, Luminescent Materials, Springer-Verlag New Yor Berlin Heidelberg (1994).

[5] G. H. Dieke, Spectra and Energy Levels of Rare Earth Ions in Crystals, Interscience Publishers. New York (1968).

[6] S. Shionoya and W. M. Yen, Phosphor Handbook, CRC Press, Boca Raton, FL (1999).

[7] E. Downing, L. Hesselink, J. Ralston and R. Macfarlane, Science 273 (1996) 1185.

[8] H. Berthou and C. K. Jörgensen, Optics Letters 15 (1990) 1100.

[9] G. S. Yi, H. C. Lu, S. Y. Zhao, G. Yue, W. J. Yang, D. P. Chen and L. H. Guo, Nano Letters 4 (2004) 2191.

[10] S. Heer, K. Kompe, H. U. Gudel and M. Haase, Advanced Materials 16 (2004) 2102.

[11] Y.-W. Zhang, X. Sun, R. Si, L.-P. You and C.-H. Yan, Journal of the American Chemical Society 127 (2005) 3260.

[12] L. Y. Wang and Y. D. Li, Nano Letters 6 (2006) 1645.

[13] X. Wang, J. Zhuang, Q. Peng and Y. D. Li, Nature 437 (2005) 121.

[14] A. Aebischer, S. Heer, D. Biner, K. Kramer, M. Haase and H. U. Gudel, Chemical Physics Letters 407 (2005) 124.

[15] P. Ptacek, H. Schafer, K. Kompe and M. Haase, Advanced Functional Materials 17 (2007) 3843.

[16] H. Schafer, P. Ptacek, K. Kompe and M. Haase, Chemistry of Materials 19 (2007) 1396.

[17] H. Schafer, P. Ptacek, O. Zerzouf and M. Haase, Advanced Functional Materials 18 (2008) 2913.

[18] G. S. Yi and G. M. Chow, Journal of Materials Chemistry 15 (2005) 4460.

[19] G. S. Yi and G. M. Chow, Advanced Functional Materials 16 (2006) 2324.

[20] G. S. Yi and G. M. Chow, Chemistry of Materials 19 (2007) 341.

[21] G. S. Yi, W. B. Lee and G. M. Chow, Journal of Nanoscience and Nanotechnology 7 (2007) 2790.

[22] Y. Wei, F. Q. Lu, X. R. Zhang and D. P. Chen, Chemistry of Materials 18 (2006) 5733.

[23] Y. Wei, F. Q. Lu, X. R. Zhang and D. P. Chen, Materials Letters 61 (2007) 1337.

[24] Y. Wei, F. Q. Lu, X. R. Zhang and D. P. Chen, Journal of Alloys and Compounds 427 (2007) 333.

[25] C. H. Liu, J. Sun, H. Wang and D. Chen, Scripta Materialia 58 (2008) 89.

[26] Y. Wei, F. Q. Lu, X. R. Zhang and D. P. Chen, Journal of Alloys and Compounds 455 (2008) 376.

[27] C. Liu, H. Wang, X. Li and D. Chen, Journal of Materials Chemistry 19 (2009) 3546.

[28] J. C. Boyer, F. Vetrone, L. A. Cuccia and J. A. Capobianco, Journal of the American Chemical Society 128 (2006) 7444.

[29] J. C. Boyer, J. Gagnon, L. A. Cuccia and J. A. Capobianco, Chemistry of Materials 19 (2007) 3358.

[30] V. Mahalingam, F. Mangiarini, F. Vetrone, V. Venkatramu, M. Bettinelli, A. Speghini and J. A. Capobianco, Journal of Physical Chemistry C 112 (2008) 17745.

[31] K. A. Abel, J.-C. Boyer and F. C. J. M. v. Veggel, Journal of the American Chemical Society 131 (2009) 14644.

[32] V. Mahalingam, F. Vetrone, R. Naccache, A. Speghini and J. A. Capobianco, Advanced Materials 21 (2009) 4025.

[33] R. Naccache, F. Vetrone, V. Mahalingam, L. A. Cuccia and J. A. Capobianco, Chemistry of Materials 21 (2009) 717.

[34] F. V. Venkataramanan Mahalingam, Rafik Naccache, Adolfo Speghini and a. J. A. Capobianco*, Journal of Materials Chemistry 19 (2009) 3093.

[35] F. Vetrone, V. Mahalingam and J. A. Capobianco, Chemistry of Materials 21 (2009) 1847.

[36] F. Vetrone, R. Naccache, V. Mahalingam, C. G. Morgan and J. A. Capobianco, Advanced Functional Materials 19 (2009) NA.

[37] Z. L. Wang, Z. W. Quan, P. Y. Jia, C. K. Lin, Y. Luo, Y. Chen, J. Fang, W. Zhou, C. J. O'Connor and J. Lin, Chemistry of Materials 18 (2006) 2030.

[38] Y. Jin, W. P. Qin and J. S. Zhang, Journal of Fluorine Chemistry 129 (2008) 515.

[39] C. Li, X. Liu, P. Yang, C. Zhang, H. Lian and J. Lin, Journal of Physical Chemistry C 112 (2008) 2904.

[40] C. X. Li, J. Yang, P. P. Yang, H. Z. Lian and J. Lin, Chemistry of Materials 20 (2008) 4317.

[41] Z. W. Quan, D. M. Yang, P. P. Yang, X. M. Zhang, H. Z. Lian, X. M. Liu and J. Lin, Inorganic Chemistry 47 (2008) 9509.

[42] Z. Q. Xiaoming Zhang, Jun Yang, Piaoping Yang, Hongzhou Lian and J. Lin, Nanotechnology 19 (2008) 075603.

[43] Z. Quan, P. Yang, C. Li, J. Yang, D. Yang, Y. Jin, H. Lian, H. Li and J. Lin, The Journal of Physical Chemistry C 0 (2009).

[44] F. Wang and X. G. Liu, Journal of the American Chemical Society 130 (2008) 5642.

[45] H.-X. Mai, Y.-W. Zhang, R. Si, Z.-G. Yan, L.-d. Sun, L.-P. You and C.-H. Yan, Journal of the American Chemical Society 128 (2006) 6426.

[46] Y.-P. Du, X. Sun, Y.-W. Zhang, Z.-G. Yan, L.-D. Sun and C.-H. Yan, Crystal Growth & Design 9 (2009) 2013.

[47] W. Feng, L. D. Sun and C. H. Yan, Chemical Communications (2009) 4393.

[48] P. Li, Q. Peng and Y. Li, Advanced Materials 21 (2009) 1945.

[49] G. Wang, Q. Peng and Y. Li, Journal of the American Chemical Society 131 (2009) 14200.

[50] T. Xie, S. A. Li, Q. Peng and Y. D. Li, Angewandte Chemie-International Edition 48 (2009) 196.

[51] Y. Z. Zhengquan Li, Angewandte Chemie International Edition 45 (2006) 7732.

[52] Z. Li, Y. Zhang and S. Jiang, Advanced Materials 20 (2008) 4765.

[53] H. S. Qian and Y. Zhang, Langmuir 24 (2008) 12123.

[54] G. A. Kumar, C. W. Chen, J. Ballato and R. E. Riman, Chemistry of Materials 19 (2007) 1523.

[55] C. Feldmann, M. Roming and K. Trampert, Small 2 (2006) 1248.

[56] Y. Y. Zhang, L. W. Yang, C. F. Xu, J. X. Zhong and C. Q. Sun, Applied Physics B-Lasers and Optics 98 (2010) 243.

[57] S. F. Lim, R. Riehn, W. S. Ryu, N. Khanarian, C.-k. Tung, D. Tank and R. H. Austin, Nano Letters 6 (2005) 169.

[58] L. Y. Wang, R. X. Yan, Z. Y. Hao, L. Wang, J. H. Zeng, H. Bao, X. Wang, Q. Peng and Y. D. Li, Angewandte Chemie-International Edition 44 (2005) 6054.

[59] P. Zhang, S. Rogelj, K. Nguyen and D. Wheeler, Journal of the American Chemical Society 128 (2006) 12410.

[60] L. N. Sun, H. S. Peng, M. I. J. Stich, D. Achatz and O. S. Wolfbeis, Chemical Communications (2009) 5000.

[61] A. Shalav, B. S. Richards, T. Trupke, K. W. Kramer and H. U. Gudel, Applied Physics Letters 86 (2005) 3.

[62] T. Trupke, A. Shalav, B. S. Richards, P. Würfel and M. A. Green, Solar Energy Materials and Solar Cells 90 (2006) 3327.

[63] R. Y. Tsien, Annual Review of Biochemistry 67 (1998) 509.

[64] I. L. Medintz, H. T. Uyeda, E. R. Goldman and H. Mattoussi, Nature Materials 4 (2005) 435.

[65] J. Shen, L. D. Sun and C. H. Yan, Dalton Transactions (2008) 5687.

[66] N. C. Shaner, R. E. Campbell, P. A. Steinbach, B. N. G. Giepmans, A. E. Palmer and R. Y. Tsien, Nature Biotechnology 22 (2004) 1567.

[67] H. J. Moon, K. N. Kim, K. M. Kim, S. H. Choi, C. K. Kim, K. D. Kim, R. Z. LeGeros and Y. K. Lee, Journal of Biomedical Materials Research Part A 74A (2005) 497.

[68] S. E. Hatch, R. J. Weagley and W. F. Parsons, Applied Physics Letters 5 (1964) 153.

[69] X. M. Sun and Y. D. Li, Chemical Communications (2003) 1768.

[70] R. D. Shannon, Acta Crystallographica, Section A: Crystal Physics, Diffraction, Theoretical and General Crystallography A32 (1976) 751.

[71] M. A. Hines and P. Guyot-Sionnest, The Journal of Physical Chemistry 100 (1996) 468.

[72] B. O. Dabbousi, J. Rodriguez-Viejo, F. V. Mikulec, J. R. Heine, H. Mattoussi, R. Ober, K. F. Jensen and M. G. Bawendi, The Journal of Physical Chemistry B 101 (1997) 9463.

[73] X. Peng, M. C. Schlamp, A. V. Kadavanich and A. P. Alivisatos, Journal of the American Chemical Society 119 (1997) 7019.

[74] Z. G. Yan and C. H. Yan, Journal of Materials Chemistry 18 (2008) 5046.

[75] P. Rahman and M. Green, Nanoscale 1 (2009) 214.

[76] W. Feng, L. D. Sun, Y. W. Zhang and C. H. Yan, Coordination Chemistry Reviews 254 1038.

[77] A. Bensalah, M. Mortier, G. Patriarche, P. Gredin and D. Vivien, Journal of Solid State Chemistry 179 (2006) 2636.

[78] P. Dorenbos and H. W. Den Hartog, Physical Review B 31 (1985) 3932.

[79] M. Kusatsugu, M. Kanno, T. Honma and T. Komatsu, Journal of Solid State Chemistry 181 (2008) 1176.

[80] P. Aubry, A. Bensalah, P. Gredin, G. Patriarche, D. Vivien and M. Mortier, Optical Materials 31 (2009) 750.

[81] J. E. Roberts, Journal of the American Chemical Society 83 (2002) 1087.

[82] S. G. Kwon, Y. Piao, J. Park, S. Angappane, Y. Jo, N.-M. Hwang, J.-G. Park and T. Hyeon, Journal of the American Chemical Society 129 (2007) 12571.

[83] A. R. Kortan, R. Hull, R. L. Opila, M. G. Bawendi, M. L. Steigerwald, P. J. Carroll and L. E. Brus, Journal of the American Chemical Society 112 (1990) 1327.

[84] D. Yuan, G. S. Yi and G. M. Chow, Journal of Materials Research 24 (2009) 2042.

[85] J. F. Suyver, A. Aebischer, D. Biner, P. Gerner, J. Grimm, S. Heer, K. W. Kramer, C. Reinhard and H. U. Gudel, Optical Materials 27 (2005) 1111.

[86] G. Drazic, S. Kobe, A. C. Cefalas, E. Sarantopoulou and Z. Kollia, in 4th International Workshop on Nanoscience and Nanotechnologies (Thessaloniki, GREECE, 2007) p. 119.

[87] D. J. Cherniak, X. Y. Zhang, N. K. Wayne and E. B. Watson, Chemical Geology 181 (2001) 99.

[88] K. K. Nanda, A. Maisels, F. E. Kruis, H. Fissan and S. Stappert, Physical Review Letters 91 (2003) 106102.

[89] W. Stober, A. Fink and E. Bohn, Journal of Colloid and Interface Science 26 (1968) 62.

[90] F. J. Arriagada and K. Osseoasare, Colloids and Surfaces 69 (1992) 105.

[91] S. T. Selvan, T. T. Tan and J. Y. Ying, Advanced Materials 17 (2005) 1620.

[92] M. Stjerndahl, M. Andersson, H. E. Hall, D. M. Pajerowski, M. W. Meisel and R. S. Duran, Langmuir 24 (2008) 3532.

[93] Qian, L. P., D. Yuan, G.S. Yi and G. M. Chow, Journal of Materials Research 24(2009) 3559-3568